

Compact finite volume schemes on boundary-fitted grids

M. Piller^{a,*}, E. Stalio^b

^a *Dipartimento di Ingegneria Civile ed Ambientale – Sezione Georisorse, Università degli Studi di Trieste, Via A. Valerio, 6/1, 34127 Trieste, Italy*

^b *Dipartimento di Ingegneria Meccanica e Civile, Università di Modena e Reggio Emilia, Via Vignolese, 905/B, 41100 Modena, MO, Italy*

Received 16 October 2006; received in revised form 21 December 2007; accepted 16 January 2008

Available online 26 January 2008

Abstract

The paper focuses on the development of a framework for high-order compact finite volume discretization of the three-dimensional scalar advection–diffusion equation. In order to deal with irregular domains, a coordinate transformation is applied between a curvilinear, non-orthogonal grid in the physical space and the computational space. Advective fluxes are computed by the fifth-order upwind scheme introduced by Pirozzoli [S. Pirozzoli, Conservative hybrid compact-WENO schemes for shock–turbulence interaction, *J. Comp. Phys.* 178 (2002) 81] while the Coupled Derivative scheme [M.H. Kobayashi, On a class of Padé finite volume methods, *J. Comp. Phys.* 156 (1999) 137] is used for the discretization of the diffusive fluxes.

Numerical tests include unsteady diffusion over a distorted grid, linear free-surface gravity waves in a irregular domain and the advection of a scalar field. The proposed methodology attains high-order formal accuracy and shows very favorable resolution characteristics for the simulation of problems with a wide range of length scales.

© 2008 Elsevier Inc. All rights reserved.

PACS: 65C20; 65M99

Keywords: Coupled Derivative scheme; Finite volume; Curvilinear grids; Advection–diffusion equation

1. Introduction

High-order compact finite difference schemes are widely used in direct and large eddy simulation of turbulent flows and in aeroacoustics [19]. The application of compact schemes to the finite volume discretization is more involving, since it requires the development of high-order procedures for the approximation of fluxes and volume integrals. Finite volume compact schemes have not yet been applied in simulations of practical interest, but there is a number of studies where finite volume compact discretization schemes are developed and examined.

* Corresponding author. Tel.: +39 040 5587896; fax: +39 040 5583497.

E-mail addresses: piller@univ.trieste.it, piller@units.it (M. Piller), enrico.stalio@unimore.it (E. Stalio).

Kobayashi [12] deals with fundamental issues on implicit spatial discretization schemes, like the interpretation of compact finite difference and finite volume schemes in the framework of Hermite interpolation, the dispersion and diffusion characteristics of compact schemes, the effect of boundary stencils on the global accuracy and resolution of the method. It is shown that the combination of a third-order boundary scheme with a fourth-order Padé internal scheme yields only third-order accuracy for the computed reflection ratio, for the one-dimensional linear wave equation. As confirmed in the paper by Kwok et al. [13], a sufficient condition to keep a high order truncation accuracy is to use boundary schemes at least as accurate as the interior schemes.

The development and implementation of finite volume compact scheme algorithms in Cartesian coordinate system, is described in the papers by Pereira et al. [24] for collocated grids and Piller et al. [25] for the staggered arrangement of variables. In both cases space averaged values and fluxes are regarded as main unknowns, but cell-averaged values are not mistaken with pointwise values as wrongly stated in Ref. [32], and the solutions achieve the expected high order accuracy. Pereira et al. [24] point out the advantages of the finite volume representation of Dirichlet boundaries compared to finite difference schemes, in that an unstable downwind extrapolation is not required. The possibility to extend the proposed methodology to curvilinear coordinates, using a coordinate mapping, is mentioned but not pursued by Pereira and coworkers.

Lacor et al. [17] introduce second-order compact finite volume schemes for boundary-fitted grids that are developed directly in physical space. This approach is well suited for highly-irregular grids because of the suppression of the error associated with the discrete representation of metric terms [6]. Nevertheless, the development of high-order schemes is rather cumbersome and the calculation of compact interpolants and differences can not be decoupled along single coordinate directions. Results are reported for several one- and two-dimensional simulations and a three-dimensional large eddy simulation of turbulent channel flow. A coordinate mapping is used to deal with irregular grids in the work by Sengupta et al. [28], where a new flux-vector splitting compact finite volume scheme for the linear wave equation is introduced, but the methodology is developed and validated in one dimension.

While compact finite difference schemes have been successfully used for simulations in complex geometries [6,11,29,15,31], compact finite volume simulations have appeared only for two- and three-dimensional Cartesian grids or simple two-dimensional curvilinear grids. However, Mattiussi [23] proves by topological arguments that integral methods, like finite volumes and finite elements, are more suitable for the numerical simulation of field problems and Popescu et al. [27] verify by numerical experiments that finite volume methods are superior to their finite difference counterpart in the inviscid advection of discontinuities.

The present paper reports on the application of the compact finite volume method on curvilinear non-orthogonal grids in three dimensions. The focus is on the scalar advection–diffusion equation, which is a mathematical model for several physical phenomena like thermal diffusion, laminar flow through porous media, the propagation of surface gravity waves and the transfer of contaminants through the atmosphere. The Coupled Derivative scheme (C-D hereafter) [12] and the fifth-order upwind compact scheme by Pirozzoli [26] are used for the approximation of the diffusive and advective fluxes, respectively, and their resolution properties investigated by Fourier and eigenvalue analysis.

2. Mathematical and numerical formulation

2.1. Mathematical formulation

The scalar advection–diffusion equation with arbitrary boundary conditions which is numerically solved in the present article reads

$$\begin{cases} \frac{\partial \varphi}{\partial t} + \nabla \cdot (\mathbf{u}\varphi) = \nabla \cdot [\alpha(\mathbf{x}, t, \varphi)\nabla\varphi] + S & \text{in } \overset{\circ}{\Omega} \\ B(\mathbf{x}, t, \varphi, \frac{\partial \varphi}{\partial n}) = 0 & \text{on } \partial\Omega \end{cases} \quad (1)$$

where \mathbf{u} is the velocity, α the diffusion coefficient, S a source term and the function B represents general boundary conditions. The domain of interest in physical space Ω can be of any shape, provided it can be mapped onto a cubic domain ω in the computational space. The computational domain is subdivided by a uniform

Cartesian mesh, which maps onto a distorted grid in the physical space, as sketched in Fig. 1 for the two-dimensional case. For coordinate transformations, the following nomenclature is used:

- $\mathbf{x}(\xi)$ is the coordinate transformation between the physical (\mathbf{x}) and the computational (ξ) space.
- $\mathbf{J} := (\partial\mathbf{x}/\partial\xi)$ is the Jacobian matrix of the coordinate transformation
- $J := \det(\mathbf{J})$
- \mathbf{E}_i and \mathbf{E}^i are the covariant and contravariant basis vectors, respectively.
- $\underline{\mathbf{g}}$ and $\overline{\mathbf{g}}$ are the covariant and contravariant metric tensors, respectively.
- u^i are the contravariant velocity components.

In the framework of finite volume methods, the governing equations are integrated over each control volume in physical space. Integration of Eq. (1) yields

$$\begin{aligned} \frac{d}{dt} \int \int \int_{\Delta\omega} \varphi J d\xi + (\widehat{\Phi}_1^{\rightarrow} + \widehat{\Phi}_1^{\leftarrow}) + (\widehat{\Phi}_2^{\rightarrow} + \widehat{\Phi}_2^{\leftarrow}) + (\widehat{\Phi}_3^{\rightarrow} + \widehat{\Phi}_3^{\leftarrow}) \\ = (\Phi_1^{\rightarrow} + \Phi_1^{\leftarrow}) + (\Phi_2^{\rightarrow} + \Phi_2^{\leftarrow}) + (\Phi_3^{\rightarrow} + \Phi_3^{\leftarrow}) + \int \int \int_{\Delta\omega} S J d\xi \end{aligned} \tag{2}$$

where the superscript \rightarrow means that the quantity is calculated at the right, north or top boundary while the opposite is true for \leftarrow . The advective and diffusive fluxes across the control volume coordinate surfaces are defined as

$$\widehat{\Phi}_i^{\rightarrow} = + \int_{\Delta\xi_k} \int_{\Delta\xi_j} u^i \varphi J d\xi_j d\xi_k \tag{3}$$

$$\widehat{\Phi}_i^{\leftarrow} = - \int_{\Delta\xi_k} \int_{\Delta\xi_j} u^i \varphi J d\xi_j d\xi_k \tag{4}$$

$$\Phi_i^{\rightarrow} = + \int_{\Delta\xi_k} \int_{\Delta\xi_j} \alpha \frac{\partial\varphi}{\partial\xi_r} g^{ri} J d\xi_j d\xi_k \tag{5}$$

$$\Phi_i^{\leftarrow} = - \int_{\Delta\xi_k} \int_{\Delta\xi_j} \alpha \frac{\partial\varphi}{\partial\xi_r} g^{ri} J d\xi_j d\xi_k \tag{6}$$

for $i \neq j, j \neq k$ and $k \neq i$.

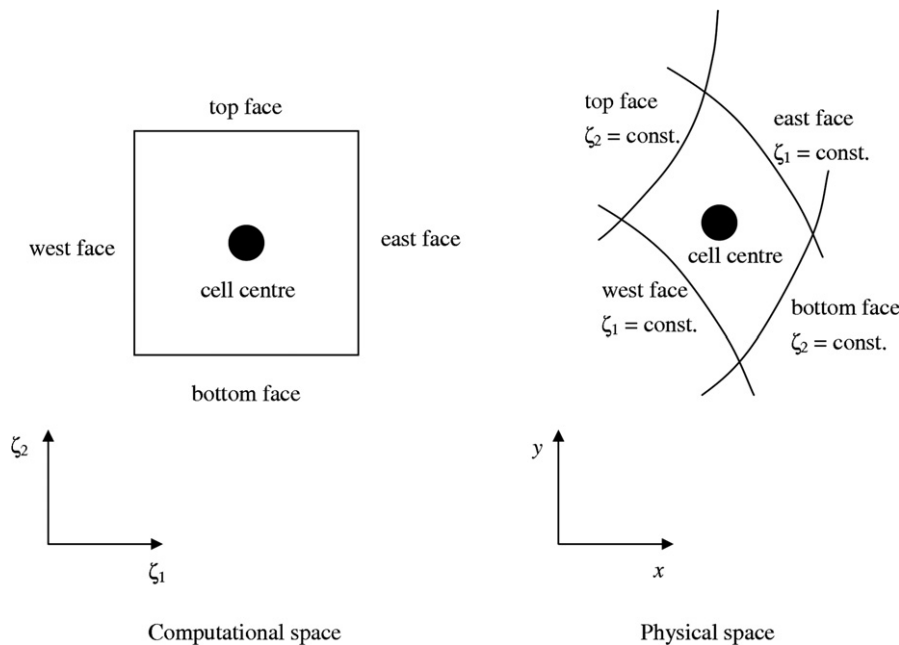


Fig. 1. Control volumes in the computational and physical control volumes.

2.2. Numerical formulation

2.2.1. Spatial discretization

2.2.1.1. *Field compact schemes.* In the present work, the advective fluxes are computed by the conservative fifth-order upwind finite difference scheme proposed by Pirozzoli [26] while the Coupled Derivative finite volume schemes by Kobayashi [12] are used to approximate the diffusive fluxes. Due to the increased number of free parameters C-D schemes attain a higher formal accuracy and better resolution characteristics as compared to standard Padé scheme [21,12].

The interpolant and first derivative of a sufficiently smooth function $\varphi(x)$ are approximated by C-D schemes from the cell-averaged values $\bar{\varphi}$ as follows:

$$\sum_{k=-m_1}^{m_2} \alpha_{j,k} \varphi_{j+k+1/2} + h \sum_{k=-p_1}^{p_2} \beta_{j,k} \varphi'_{j+k+1/2} = \sum_{k=-n_1}^{n_2} \gamma_{j,k} \bar{\varphi}_{j+k} \tag{7}$$

where h is the uniform grid spacing. Fig. 2 shows the arrangement of the various quantities appearing in Eq. (7). The fictitious cells which are used to enforce the boundary conditions are indexed as $j = 0$ (beyond the left boundary) and $j = N + 1$ (beyond the right boundary), where N is the number of internal control volumes. The positive integers $m_1, m_2, n_1, n_2, p_1, p_2$ define the width of the computational stencil, with symmetric schemes corresponding to $m_1 = m_2, p_1 = p_2, n_1 = n_2 - 1$. In this work, a sixth-order symmetric scheme is used for $j = 1, \dots, N - 1$. It is based on the following stencil

$$m_1 = m_2 = n_2 = p_1 = p_2 = 1 \quad n_1 = 0$$

As suggested by Mahesh [21], the coefficients in Eq. (7) are evaluated by alternatively setting $(\alpha_{j,0}, \beta_{j,0}) = (1, 0)$ and $(\alpha_{j,0}, \beta_{j,0}) = (0, 1)$ and two equations are obtained for each cell:

$$\begin{aligned} \sum_{k=-m_1}^{m_2} \alpha_{j,k}^{(1)} \varphi_{j+k+1/2} + h \sum_{k=-p_1}^{p_2} \beta_{j,k}^{(1)} \varphi'_{j+k+1/2} &= \sum_{k=-n_1}^{n_2} \gamma_{j,k}^{(1)} \bar{\varphi}_{j+k} \\ \sum_{k=-m_1}^{m_2} \alpha_{j,k}^{(2)} \varphi_{j+k+1/2} + h \sum_{k=-p_1}^{p_2} \beta_{j,k}^{(2)} \varphi'_{j+k+1/2} &= \sum_{k=-n_1}^{n_2} \gamma_{j,k}^{(2)} \bar{\varphi}_{j+k} \end{aligned} \tag{8}$$

A Taylor expansion analysis yields the following values [12]:

$$\begin{aligned} \alpha_{j,0}^{(1)} = 1 \quad \alpha_{j,\pm 1}^{(1)} = 0.4375 \quad \beta_{j,0}^{(1)} = 0 \quad \beta_{j,\pm 1}^{(1)} = \mp 0.0625 \quad \gamma_{j,0}^{(1)} = \gamma_{j,1}^{(1)} = 0.9375 \\ \alpha_{j,0}^{(2)} = 0 \quad \alpha_{j,\pm 1}^{(2)} = \pm 1.125 \quad \beta_{j,0}^{(2)} = 1 \quad \beta_{j,\pm 1}^{(2)} = -0.125 \quad \gamma_{j,0}^{(2)} = -\gamma_{j,1}^{(2)} = -3 \end{aligned}$$

For the representation of the advective fluxes, Pirozzoli [26] combines the fifth-order upwind finite difference compact scheme with a WENO scheme. Due to the conservativity constraint which is also enforced, the schemes devised in Ref. [26] can be directly employed in the finite volume context of the present study by replacing the point values with cell-averaged quantities:

$$3\varphi_{j-1/2} + 6\varphi_{j+1/2} + \varphi_{j+3/2} = \frac{1}{3}\bar{\varphi}_{j-1} + \frac{19}{3}\bar{\varphi}_j + \frac{10}{3}\bar{\varphi}_{j+1} \tag{9}$$

Eq. (9) is meant for the inner points of the domain and positive phase velocity.

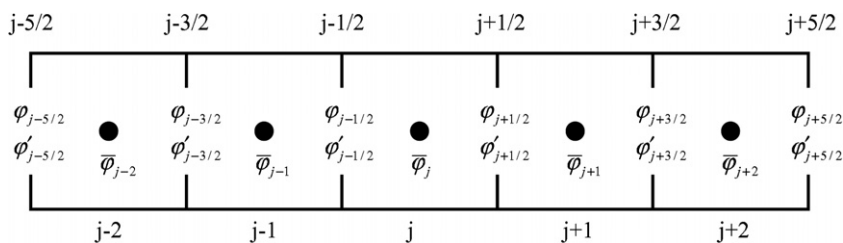


Fig. 2. Placement of discrete quantities in one-dimensional computational space.

2.2.1.2. Schemes for the boundaries. The symmetric schemes of Eqs. (8) and (9) can only be used in the interior nodes of non-periodic domains while special schemes with asymmetric stencil for both differentiation and interpolation are to be used as the boundary is approached. In this work the boundary conditions are enforced by introducing a single layer of fictitious cells surrounding the computational domain in transformed space. A similar treatment is used, among others, by Pirozzoli [26] in the context of compact finite difference approximations. Fictitious cells in physical space do not need to be defined, avoiding any ambiguity in their actual shape. The $\bar{\varphi}$ values in the fictitious cell of the transformed space become additional unknowns, with the discretized boundary conditions as corresponding equations. This technique allows an easy implementation of complicated boundary conditions especially when residual-based solvers are used, like the Newton–Krylov methods [24].

Both explicit and compact asymmetric schemes have been used in conjunction with compact schemes for the inner points. Compact one-sided schemes are considered, among others, by Lele [18], Kobayashi [12], Piller et al. [25], Boersma [2] and Jordan [16]. Explicit schemes are preferred, among others, by Hixon [9] and Pirozzoli [26]. In the present work we use explicit one-sided schemes.

The reason for this is that implicit schemes in combination with the interior C-D scheme lead to coefficient matrices which are poorly conditioned. This is shown in Fig. 3, where the inverse of the norm-1 coefficient matrix condition number is plotted as a function of the number of control volumes N . The fourth-order, periodic finite volume Padé schemes for interpolation and first derivative, introduced in Ref. [12], attain the highest asymptotic condition numbers for very small numbers of cells. The periodic sixth-order C-D (C-D6 hereafter) scheme shows a linear increase of the condition number. The explicit boundary schemes used in the present work causes a negligible increase of the condition number, with respect to the periodic case, while introduction of implicit sixth- or eight-order boundary schemes leads to ill-conditioned problems. The reason for the different condition number behavior should be related to the appearance of the grid spacing h in the coefficient matrix of the C-D schemes; it can be readily shown from Eq. (8) that as $h \rightarrow 0$ the coefficient matrix tends toward a singular matrix.

Many different combinations of interior schemes and boundary stencils can be found in the literature. Following Gustafsson [8], for hyperbolic problems, boundary schemes one order lower than the interior ensure global convergence consistent with the order of the interior scheme. Although this feature was verified numerically by Pirozzoli [26] for his method, we already mentioned in Section 1 that Kobayashi [12] and Kwok et al. [13] came to different conclusions. Kobayashi [12], based on results of a finite volume

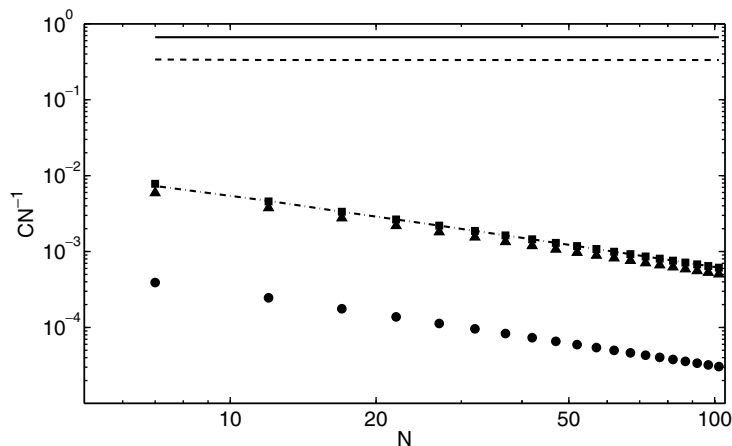


Fig. 3. Inverse of the norm-1 condition number of the coefficient matrix for various compact interpolation and first-difference schemes. Solid line: periodic CS4 for first derivative [25]; dashed line: periodic CS4 for interpolation [25]; dot-dash: periodic sixth-order C-D scheme [12]; squares: sixth-order C-D scheme with present explicit boundary schemes; triangles: sixth-order C-D scheme with sixth-order implicit boundary schemes; bullets: sixth-order C-D scheme with eighth-order implicit boundary schemes.

simulation of the one-dimensional, steady advection–diffusion equation, shows that the quality of solutions obtained with C-D schemes is even more affected by the boundary closure than for traditional Padé schemes, and that for C-D schemes the overall order of accuracy is given by the near-boundary compact schemes. On the other hand, Mahesh [21] develops templates formed by a sixth-order symmetric C-D finite difference scheme in the interior and third-, fourth- or fifth-order C-D boundary schemes and verifies numerically that only the third-order scheme results in asymptotically stable solutions of the one-dimensional linear advection equation.

In the present work, the explicit schemes used next to the boundaries are at least of the same order of accuracy as the interior schemes.

For the discretization of the advective term next to the boundaries, fourth-order, explicit, one-sided boundary schemes are used in the present work, as introduced in Ref. [26]. For positive phase speed they result

$$\varphi_{1/2} = \frac{1}{4}\bar{\varphi}_0 + \frac{13}{12}\bar{\varphi}_1 - \frac{5}{12}\bar{\varphi}_2 + \frac{1}{12}\bar{\varphi}_3 \tag{10}$$

$$\varphi_{N+1/2} = \frac{25}{12}\bar{\varphi}_N - \frac{23}{12}\bar{\varphi}_{N-1} + \frac{13}{12}\bar{\varphi}_{N-2} - \frac{1}{4}\bar{\varphi}_{N-3} \tag{11}$$

The approximation (10) is used at inflow boundaries, while (11) applies at outflow boundaries. Since (11) does not include the fictitious cell, which however is considered as unknown in the present work, care is taken in order to avoid that the system of equations becomes singular.

2.2.1.3. Deconvolution. As stated in Ref. [22], deconvolution is the restoration of signals degraded by a convolution operator. In the context of high-order finite volume discretization, deconvolution is required in order to recover a pointwise representation of a quantity from the knowledge of its mean values over a set of control volumes. This distinction is unnecessary for second-order finite volume discretization but becomes substantial when high-order schemes are employed. While Pereira et al. [24] and Piller et al. [25] use compact deconvolution schemes, in the present work explicit schemes are preferred because they can be more easily adapted to the desired order of accuracy.

With reference to the one-dimensional case, the aim is to recover $f(\xi)$ from knowledge of $\bar{f}(\xi)$, where

$$\bar{f}(\xi) = \frac{1}{\Delta\xi} \int_{\xi-\Delta\xi/2}^{\xi+\Delta\xi/2} f(\zeta) d\zeta \tag{12}$$

Let us assume that the values $\bar{f}_i, \bar{f}_{i+1}, \dots, \bar{f}_{i+m}$ are known and we aim to approximate $f(\xi)$ at some point ξ . To this end, we expand f as

$$f(\xi) \approx \hat{f}(\xi) = \sum_{j=0}^m a_j P_j(\xi)$$

where $\{P_j(\xi)\}_{j=0}^m$ is a set of linearly-independent polynomials with P_j of order j and \hat{f} is an approximation to f . The $m + 1$ conditions

$$\bar{f}_{i+k} = \bar{f}_{i+k}, \quad k = 0, 1, \dots, m \tag{13}$$

allow to compute the coefficients a_j . Eq. (13) can be written in matrix form:

$$\bar{\mathbf{f}} = \bar{\mathbf{P}}\mathbf{a} \tag{14}$$

where

$$\bar{\mathbf{P}} := [\bar{P}_i^j]; \quad \bar{P}_i^j := \frac{1}{\Delta\xi} \int_{\xi^*-\Delta\xi/2}^{\xi^*+\Delta\xi/2} P_j(\zeta) d\zeta$$

and the approximated value $\hat{f}(\xi^*)$ can be computed by

$$\hat{f}(\xi^*) = \sum_j P_j(\xi^*) a_j = [P_0(\xi^*) \dots P_m(\xi^*)]\mathbf{a} := \mathbf{P}\mathbf{a} \tag{15}$$

with

$$\mathbf{P} := [P_0(\xi^*) \dots P_m(\xi^*)]$$

Substitution of Eq. (14) into (15) yields

$$f(\xi^*) = \mathbf{P}\bar{\mathbf{P}}^{-1}\bar{\mathbf{f}} := [\hat{g}_0(\xi^*) \dots \hat{g}_m(\xi^*)]\bar{\mathbf{f}}$$

it is apparent that the *Lagrange-like* functions $\hat{g}_j(\xi)$ may be precomputed at $\xi = \xi^*$ by solving the system (14) with $m + 1$ different right-hand sides, corresponding to the canonical unit vectors of R^{m+1} .

With regard to the existence and uniqueness of such an approximation, the problem is equivalent to finding the conditions for the coefficient matrix in Eq. (14) to be non-singular. Such conditions can be found from the theory of pointwise interpolation. The primitive function of f is introduced

$$F(\xi) := \int_0^\xi f(\eta) d\eta$$

so that

$$\bar{f}(\xi) := \frac{1}{\Delta\xi} \int_{\xi-\Delta\xi/2}^{\xi+\Delta\xi/2} f(\eta) d\eta = \frac{1}{\Delta\xi} [F(\xi + \Delta\xi/2) - F(\xi - \Delta\xi/2)]$$

Since similar definitions and identities apply to the approximation function $\hat{f}(\xi)$, conditions (13) may be recast as

$$\frac{1}{\Delta\xi} [F(\xi_k + \Delta\xi/2) - F(\xi_k - \Delta\xi/2)] = \frac{1}{\Delta\xi} [\hat{F}(\xi_k + \Delta\xi/2) - \hat{F}(\xi_k - \Delta\xi/2)] \quad \forall k = 0, \dots, m \tag{16}$$

this implies that the two sequences

$$\{F(\xi_0 - \Delta\xi/2), F(\xi_1 - \Delta\xi/2), \dots, F(\xi_m + \Delta\xi/2)\}$$

$$\{\hat{F}(\xi_0 - \Delta\xi/2), \hat{F}(\xi_1 - \Delta\xi/2), \dots, \hat{F}(\xi_m + \Delta\xi/2)\}$$

differ at most by an additive constant. Therefore, the problem of finding \hat{f} is equivalent to finding the pointwise interpolant \hat{F} to F through the $m + 1$ points $\xi_k - \Delta\xi/2, k = 1, \dots, m + 1$ while setting $\hat{F}(\xi_0 - \Delta\xi/2)$ to an arbitrary value. In the case of polynomial interpolation, such an interpolant exists and is unique as long as the $m + 1$ interpolation nodes are distinct and the degree of the interpolation polynomial is not higher than m .

Multi-dimensional deconvolution can be obtained by tensor-product of the one-dimensional interpolant basis [3]. This corresponds to interpolating independently and in sequence along each coordinate direction,

$$\hat{f}(\xi_1, \xi_2, \xi_3) = \sum_{i_3=0}^{m_3} \sum_{i_2=0}^{m_2} \sum_{i_1=0}^{m_1} \bar{f}_{i_1, i_2, i_3} \hat{g}_{i_1, q_1}(\xi_1) \hat{g}_{i_2, q_2}(\xi_2) \hat{g}_{i_3, q_3}(\xi_3) \tag{17}$$

The reconstruction of a function f onto a set of quadrature nodes can be made considerably more efficient by using the sum-factorization technique [10]. With reference to Eq. (17), the sum-factorization results in

$$\begin{aligned} \hat{f}_{q_1, q_2, q_3} &= \sum_{i_3=0}^{m_3} \sum_{i_2=0}^{m_2} \sum_{i_1=0}^{m_1} \bar{f}_{i_1, i_2, i_3} \hat{g}_{i_1, q_1} \hat{g}_{i_2, q_2} \hat{g}_{i_3, q_3} = \sum_{i_3=0}^{m_3} \hat{g}_{i_3, q_3} \sum_{i_2=0}^{m_2} \hat{g}_{i_2, q_2} \underbrace{\sum_{i_1=0}^{m_1} \hat{g}_{i_1, q_1} \bar{f}_{i_1, i_2, i_3}}_{A_{q_1, i_2, i_3}} \\ &= \sum_{i_3} \hat{g}_{i_3, q_3} \underbrace{\sum_{i_2} \hat{g}_{i_2, q_2} A_{q_1, i_2, i_3}}_{B_{q_1, q_2, i_3}} = \sum_{i_3} \hat{g}_{i_3, q_3} B_{q_1, q_2, i_3} \end{aligned} \tag{18}$$

where the indices i_1, i_2, i_3 refer to the basis functions, while q_1, q_2, q_3 identify the quadrature nodes, respectively. The sum-factorization technique reduces the complexity of the deconvolution from order 6 to order 4.

2.2.1.4. Flux representation. In this section, a high-order procedure is presented, for the discretization of diffusive and advective fluxes on non-orthogonal curvilinear grids.

Focusing on the orthogonal diffusive flux across the *east* coordinate surface ΔS_e of a control volume, the following term must be discretized:

$$\int \int_{\Delta S_e} \alpha \frac{\partial \varphi}{\partial \xi_1} g^{1,1} J d\xi_2 d\xi_3 \tag{19}$$

three integrals need to be computed for this purpose

$$\frac{1}{\Delta \xi_2 \Delta \xi_3} \int_{\Delta \xi_3} \int_{\Delta \xi_2} \alpha d\xi_2 d\xi_3 \tag{20}$$

$$\frac{1}{\Delta \xi_2 \Delta \xi_3} \int_{\Delta \xi_3} \int_{\Delta \xi_2} \frac{\partial \varphi}{\partial \xi_1} d\xi_2 d\xi_3 \tag{21}$$

$$\frac{1}{\Delta \xi_2 \Delta \xi_3} \int_{\Delta \xi_3} \int_{\Delta \xi_2} g^{1,1} J d\xi_2 d\xi_3 \tag{22}$$

Assuming that the diffusion coefficient α depends on \mathbf{x} , t and φ , it can be evaluated at the Gauss–Legendre quadrature nodes once φ has been computed at the same locations. This is achieved by applying the deconvolution procedure described in Section 2.2.1.3 to the face-averaged values of φ , which in turn are computed from the cell-averaged values by compact interpolation along ξ_1 . Then, Gauss–Legendre quadrature on the cell face yields the required approximation of (20). The second term (21) is evaluated directly by the compact interpolation scheme presented in Section 2.2.1.1. The third contribution, Eq. (22), is computed and stored after the calculation of the metric terms. Once the contributions (20) and (21) are available, the deconvolution procedure outlined in Section 2.2.1.3 is used once more to evaluate the integrand functions in Eqs. (20)–(22) at the quadrature nodes of the cell face considered. Gauss quadrature of the product of the three integrands yields the desired approximation for (19).

The discretization procedure for the cross-diffusive fluxes is presented for the term

$$\int \int_{\Delta S_e} \alpha \frac{\partial \varphi}{\partial \xi_2} g^{2,1} J d\xi_2 d\xi_3 \tag{23}$$

In order to evaluate the integral in Eq. (23), the following face-averaged contributions are needed in computational space:

$$\frac{1}{\Delta \xi_2 \Delta \xi_3} \int_{\Delta \xi_3} \int_{\Delta \xi_2} \alpha d\xi_2 d\xi_3 \tag{24}$$

$$\frac{1}{\Delta \xi_2 \Delta \xi_3} \int_{\Delta \xi_3} \int_{\Delta \xi_2} \frac{\partial \varphi}{\partial \xi_2} d\xi_2 d\xi_3 \tag{25}$$

$$\frac{1}{\Delta \xi_2 \Delta \xi_3} \int_{\Delta \xi_3} \int_{\Delta \xi_2} g^{2,1} J d\xi_2 d\xi_3 \tag{26}$$

After these expressions have been calculated, they can be used to obtain an approximation of (23) by following the same procedure outlined for the evaluation of the orthogonal diffusive fluxes. Integrals (24) and (26) are computed as (20) and (22), respectively. The diffusive term (25) can be evaluated by first integrating along ξ_2 with no approximation:

$$\frac{1}{\Delta S_e} \int \int_{\Delta S_1} \frac{\partial \varphi}{\partial \xi_2} d\xi_2 d\xi_3 = \frac{1}{\Delta \xi_3} \int_{\Delta \xi_3} \frac{\varphi_{i+1/2,j+1/2,k} - \varphi_{i+1/2,j-1/2,k}}{\Delta \xi_2} d\xi_3 = \frac{\overline{\varphi}_{i+1/2,j+1/2,k}^{\xi_3} - \overline{\varphi}_{i+1/2,j-1/2,k}^{\xi_3}}{\Delta \xi_2} \tag{27}$$

then, the terms $\overline{\varphi}_{i+1/2,j\pm 1/2,k}^{\xi_3}$ can be evaluated by either of two compact interpolations, along ξ_2 or along ξ_1 .

The approximation of the advective fluxes is based on the same general technique used for the diffusive fluxes. Considering the flux $\widehat{\varphi}_1^-$ defined in Eq. (3), the cell face averages of $u^1 J$ and φ are computed by the compact schemes (9)–(11). Then, the deconvolution procedure described in Section 2.2.1.3 followed by Gauss–Legendre quadrature is used to obtain the advective flux (3).

The flux representation procedure described above is used also to enforce the boundary conditions with high-order accuracy. The third-kind (Robin) boundary conditions in boundary-fitted coordinates, for a (ξ_2, ξ_3) boundary surface, yield

$$0 = \int_{\Delta\xi_3} \int_{\Delta\xi_2} \left[a_1 \frac{\partial\varphi}{\partial\xi_k} g^{k1} J + (a_2\varphi + a_3) \sqrt{g^{1,1}} J \right] d\xi_2 d\xi_3 \quad (28)$$

where in general coefficients a_1, a_2, a_3 depend on both position and time. The discrete representation of (28) is obtained following the procedure presented in Section 2.2.1.4. The resulting algebraic equation is added to the set of discretized conservation equations for the internal control volumes.

2.2.2. Fourier analysis

In this section the resolution properties of the spatial discretization schemes employed in the proposed numerical algorithm are investigated by Fourier analysis. Classical Fourier analysis [30,12] is used to access the properties of interior schemes under the assumption of periodic boundary conditions. The focus is on the C-D6 schemes used for the spatial discretization of the diffusion equation because the resolution properties of the upwind scheme used for the discretization of the advective term has been thoroughly investigated by Pirozzoli [26].

2.2.2.1. Resolution properties. The analysis is based on the one-dimensional diffusion equation with complex exponential initial conditions:

$$\begin{cases} \frac{\partial\varphi}{\partial t} = \alpha \frac{\partial^2\varphi}{\partial x^2} \\ \varphi(x, 0) = e^{ikx} \end{cases} \quad (29)$$

and periodic boundary conditions. The cell-averaged analytical solution to Eq. (29) reads

$$\bar{\varphi}_j(t) = \varphi_j(0) F(K) \exp(-FoK^2) \quad (30)$$

where k is the wavenumber, h is the uniform grid spacing, $K = kh$ is the dimensionless wavenumber, $F(K) := (2/K) \sin(K/2)$ is the transfer function between φ and $\bar{\varphi}$ [12], j is the cell index. The Fourier number is defined as $Fo = \alpha t/h^2$.

Using the mathematical manipulations detailed in Appendix A, the error function has been computed for the second-order finite volume scheme (FV2 hereafter), the fourth-order Padé finite volume scheme (CFV4 hereafter) [12], the fourth-order *spectral-like* finite volume scheme (SCFV4 hereafter) [25], the sixth-order coupled derivative finite volume scheme. Results are shown in Fig. 4.

As expected SCFV4 and C-D6 schemes show better resolution properties compared to FV2 and CFV4 and within the range of wavenumbers $1.73 \leq K \leq 2.75$ the SCFV4 scheme is superior to C-D6. While the SCFV4 and C-D6 schemes are over-diffusive over most of the wavenumber range the FV2 and the CFV4 schemes cause a reduction in the dissipation rate of the numerical solution ($E < 1$).

Following Jordan [16], a composite template is defined as one “carrying at least two different compact finite difference stencils”. For composite templates the transfer function for interpolation H and the effective wavenumber for the first derivative \tilde{K} depend on both the wavenumber K and the *nodal* location j :

$$\tilde{\varphi}_{j+1/2} := H_j(K) e^{iK(j+1/2)} \quad \tilde{\varphi}'_{j+1/2} := i\tilde{K}_j(K) e^{iK(j+1/2)}$$

The transfer function $H_j(K)$ and the effective wavenumber $\tilde{K}_j(K)$ for the composite template used in this work are shown in Fig. 5 for the nodes $j = 1/2, j = 3/2, j = 5/2$ and for the node located in the middle of the computational domain. It is apparent that the resolution properties of the composite template are negatively affected at the first three nodes near the boundary where only waves with period larger than $4h$ are accurately represented. The spectral characteristics for the mid point are coincident with those of the interior scheme, as expected.

When the composite template is used to solve the semi-discrete one-dimensional diffusion equation, the computed solution is

$$\varphi_j(t) = \varphi_j(0) e^{-\tilde{K}_j^2 Fo} \quad \tilde{K}_j^2(K) := -i \frac{K}{2 \sin(K/2)} [\tilde{K}_{j+1/2} e^{iK/2} - \tilde{K}_{j-1/2} e^{-iK/2}]$$

Thus, the resolution error can be expressed by the following quantity \tilde{K}_j^2/K^2 whose real part can be interpreted as the ratio between the effective and the true diffusivity: values larger than unity imply that the numer-

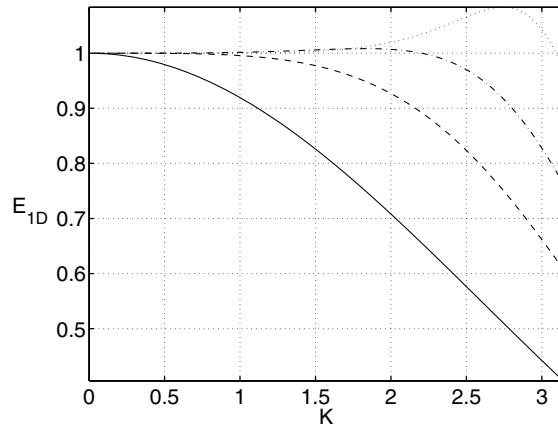


Fig. 4. Error function for the one-dimensional diffusion equation, obtained by Fourier analysis. —: FV2; ---: CFV4; -·-: SCFV4; ···: C-D6.

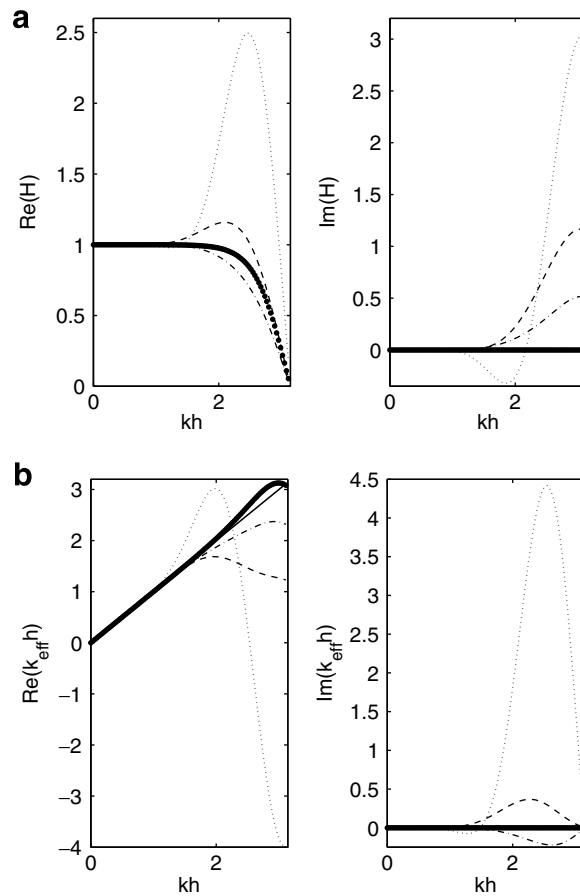


Fig. 5. (a) (Left) Real and (right) imaginary parts of the transfer function for interpolation for the composite template. (b) (Left) Real and (right) imaginary parts of the effective wavenumber for the composite template. ···: node $j = 1/2$; ---: node $j = 3/2$; -·-: node $j = 5/2$; ●●●: mid point.

ical solution decays faster than the exact solution. The imaginary part of \tilde{K}_j^2/K^2 can be recast in terms of a cell Péclet number as

$$Pe_j(K) := \frac{\tilde{c}h}{\alpha} = \frac{\text{imag}(\tilde{K}_j^2)}{K}$$

where \tilde{c} is a numerical phase velocity. Pe_j is identically zero for the exact solution and represents a dispersion error in the computed solution.

In Fig. 6, the dissipation and dispersion errors for the composite template are compared with the corresponding errors introduced by the compact finite volume fourth-order scheme and by the sixth-order C-D scheme in periodic domains. In a range of wavenumbers around $\pi/2$ and for $j = 1$ and $j = 2$, the composite template is moderately over-diffusive, it becomes highly under-diffusive in the high wavenumber range and even counter-diffusive for $K > 2.5$. This feature is in contrast with the C-D6 scheme in periodic domains, which is slightly over-diffusive. Focusing on the dispersive error, and based on the interpretation of the cell Péclet number as the ratio between the diffusive and the advective time-scales for the cell, it appears from Fig. 6 that for $j = 0$ and around $K = 2.5$ the signal is transferred about twice as fast by the numerical advection than by the true diffusion. The effect of the boundary schemes on the solution computed in the domain interior can be inferred from Fig. 7, showing the ratio between the resolution properties of the composite

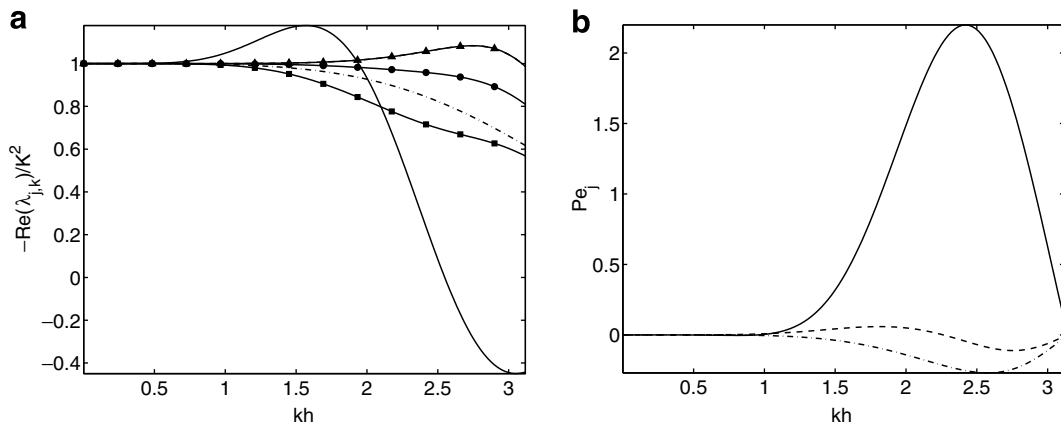


Fig. 6. (a) Dissipation error in the solution of the diffusion equation. —: composite template for the cell $j = 1$; —■—: composite template for the cell $j = 2$; —●—: composite template for the cell $j = 3$; —▲—: composite template for the cell $N/2$; - - -: sixth-order C-D scheme; - · - ·: compact fourth-order finite volume scheme. (b) Dispersion error for the composite template in the solution of the diffusion equation. —: cell $j = 1$; - - -: cell $j = 2$; - · - ·: cell $j = 3$.

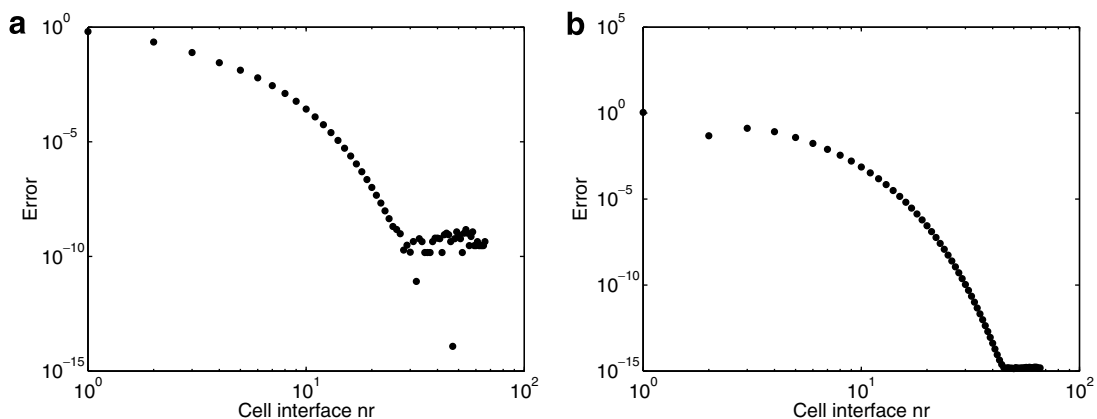


Fig. 7. Ratio between the (a) dissipation and (b) dispersion error for the composite template in the solution of the diffusive equation.

template represented in Fig. 6 with the corresponding quantities for the sixth-order C-D scheme in a periodic domain. It is evident that both the dissipation and the dispersion errors induced by the boundary schemes decay very fast when moving toward the domain interior.

2.2.2.2. *Isotropy properties.* We consider the two-dimensional diffusion equation

$$\begin{cases} \frac{\partial \varphi}{\partial t} = \alpha \left[\frac{\partial^2 \varphi}{\partial x^2} + \frac{\partial^2 \varphi}{\partial y^2} \right] \\ \varphi(x, y, 0) = e^{ik(x \cos \vartheta + y \sin \vartheta)} \end{cases} \quad (31)$$

with periodic boundary conditions. When a wavy initial solution is oriented at an angle ϑ with respect to the x axis of a Cartesian grid, the dissipation provided by a spatial discretization scheme depends on ϑ . We aim to investigate this dependence, for C-D schemes considered in the present study. As shown in Ref. [4] the two-dimensional error function becomes

$$E_{2D}(K, \vartheta) = E_{1D}(K \cos(\vartheta))[\cos(\vartheta)]^2 + E_{1D}(K \sin(\vartheta))[\sin(\vartheta)]^2 \quad (32)$$

where E_{1D} denotes the error for the one-dimensional diffusion equation, obtained in the previous section. The two-dimensional resolution error is displayed in Fig. 8. Both the C-D6 and SCFV4 schemes provide very small dissipation errors for all orientations, with the SCFV4 performing somewhat better for all represented wavenumbers except $K = 9\pi/10$ and $K = \pi$. The C-D6 scheme is over-dissipative for all wavenumbers and inclination angles, except in the highest wavenumber range for ϑ close to 0 or $\pi/2$.

2.2.3. *Effective wavenumber and eigenfunction*

When Dirichlet or Neumann boundary conditions are enforced, the Fourier analysis can no longer be used. Instead an eigenvalue analysis can be applied for homogeneous conditions. In order to investigate the resolution properties of the proposed compact schemes for elliptic problems, the eigenspectrum of the one-dimensional second-derivative is computed. This technique has been used, among others, by Kwok et al. [13] for the comparison of B-splines and compact finite difference methods.

Following the technique used by Kwok and coworkers, and thus considering the following eigenvalue problems

$$\begin{cases} v'' = \lambda v & x \in (0, 1) \\ v(0) = v(1) = 0 \end{cases} \quad \begin{cases} v'' = \lambda v & x \in (0, 1) \\ v'(0) = v'(1) = 0 \end{cases} \quad (33)$$

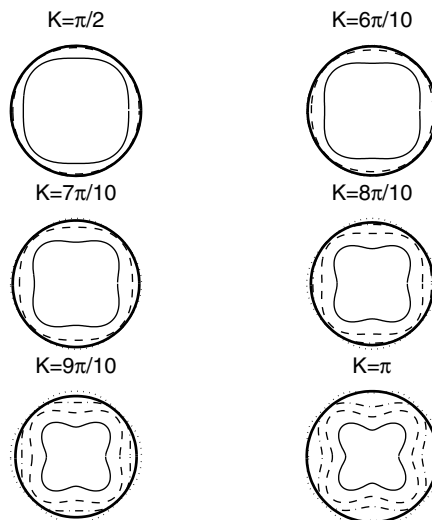


Fig. 8. Directional resolution properties for the diffusion equation. —: FV2; ---: CFV4; -·-: SCFV4; ···: C-D6. The thick solid line corresponds to the value 1.0.

The eigenvalues for both problems (33) are

$$\lambda_k = -(\pi k)^2 \tag{34}$$

once represented in the finite volume context

$$\frac{1}{h} [v'_{j+1/2} - v'_{j-1/2}] = \lambda \bar{v}_j \tag{35}$$

can be recast as

$$\mathbf{D}\bar{\mathbf{v}} = \lambda\bar{\mathbf{v}} \tag{36}$$

where the $N \times N$ matrix \mathbf{D} is modified according to the specific boundary conditions. The first-order derivatives in Eq. (35) are approximated by the FV2, the C-D6 and a 12th-order C-D finite volume scheme, C-D12 hereafter.

The relative error on the eigenvalue is reported in Fig. 9. The relative error on the eigenvalues converges as k^2 , k^6 and k^{12} for the FV2, C-D6 and C-D12 schemes, respectively. The same eigenvalues are obtained by the FV2 scheme for Dirichlet and Neumann conditions. The convergence rate of the eigenvalue is non-monotonic for both C-D schemes considered, with both boundary conditions, as already found by Kwok et al. [13] for *uncoupled* compact finite difference schemes. This effect is sensibly more pronounced for the 12th-order scheme.

The resolving efficiency for the eigenvalues $e_1(\varepsilon) := 1 - K_f/\pi$ is reported in Table 1, with threshold values of 0.1%, 1% and 10%. The C-D6 and C-D12 schemes attain considerably better results compared to the FV2 scheme, as expected. The C-D12 scheme gives poorer resolution than the C-D6 scheme, when Dirichlet boundary conditions are enforced, except in the low-wavenumber range. This effect can be ascribed to the non-monotonic convergence of the relative error for the present compact schemes.

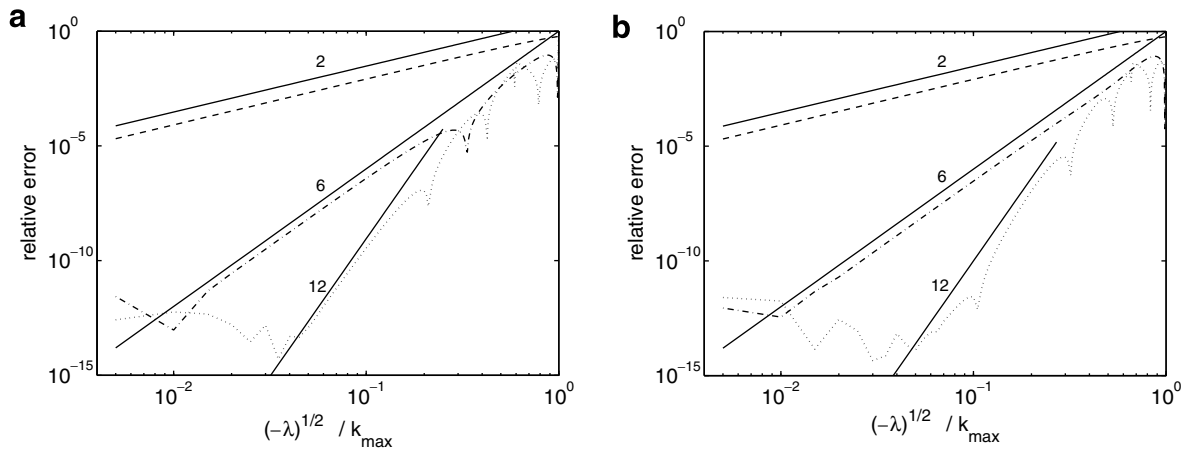


Fig. 9. Relative error in the computation of the eigenvalues for the one-dimensional heat equation with both Dirichlet and Neumann boundary conditions, on a uniform grid. The grid spacing is $h = 1/200$. (a) Dirichlet boundary conditions at both endpoints. (b) Neumann boundary conditions at both endpoints. - - -: FV2; - · - : C-D6; · · · : C-D12. Solid lines identify reference convergence rates: 2nd, 6th, 12th-order.

Table 1
Resolving efficiency for the eigenvalues of problem (33) with either Dirichlet or Neumann boundary conditions

| Scheme | $\varepsilon = 0.001$ | | $\varepsilon = 0.01$ | | $\varepsilon = 0.1$ | |
|--------|-----------------------|---------|----------------------|---------|---------------------|---------|
| | Dirichlet | Neumann | Dirichlet | Neumann | Dirichlet | Neumann |
| FV2 | 0.035 | 0.035 | 0.115 | 0.115 | 0.36 | 0.36 |
| C-D6 | 0.46 | 0.395 | 0.59 | 0.60 | 0.995 | – |
| C-D12 | 0.43 | 0.45 | 0.56 | 0.645 | 0.995 | – |

The distribution of the computed eigenvalues in the complex plane is shown in Fig. 10. The enforcement of the Dirichlet boundary conditions gives rise to two *spurious* eigenvalues, which collapse to less than the round-off error, located at a relatively large negative value on the real axis; exact values of λ/k_{\max}^2 lie between -1 and 0 . The effect of these spurious eigenvalues consists in an unphysically faster damping of the solution in time-dependent diffusion problems. This effect is more pronounced for the C-D12 scheme, as evident from Fig. 10. Two complex pairs of eigenvalues, which tend to collapse when the spatial discretization is refined, are computed for the C-D12 scheme, with both Neumann and Dirichlet boundary conditions. They cause an unphysical oscillatory damping of the solution in a time-dependent diffusion problem. In addition it was verified that the *spurious* and the complex eigenvalues correspond to eigenfunctions, which oscillate in a narrow region near the boundaries and vanish rapidly elsewhere.

3. Numerical tests

3.1. Steady two-dimensional diffusion

The two-dimensional diffusion equation is solved in a square domain $[0, 1] \times [0, 1]$ subject to the following boundary conditions:

$$\begin{aligned} \vartheta(x, y = 0) &= \vartheta(x = 0, y) = \vartheta(x = 1, y) = 0 \\ \vartheta(x, y = 1) &= \sin(\pi x) \end{aligned}$$

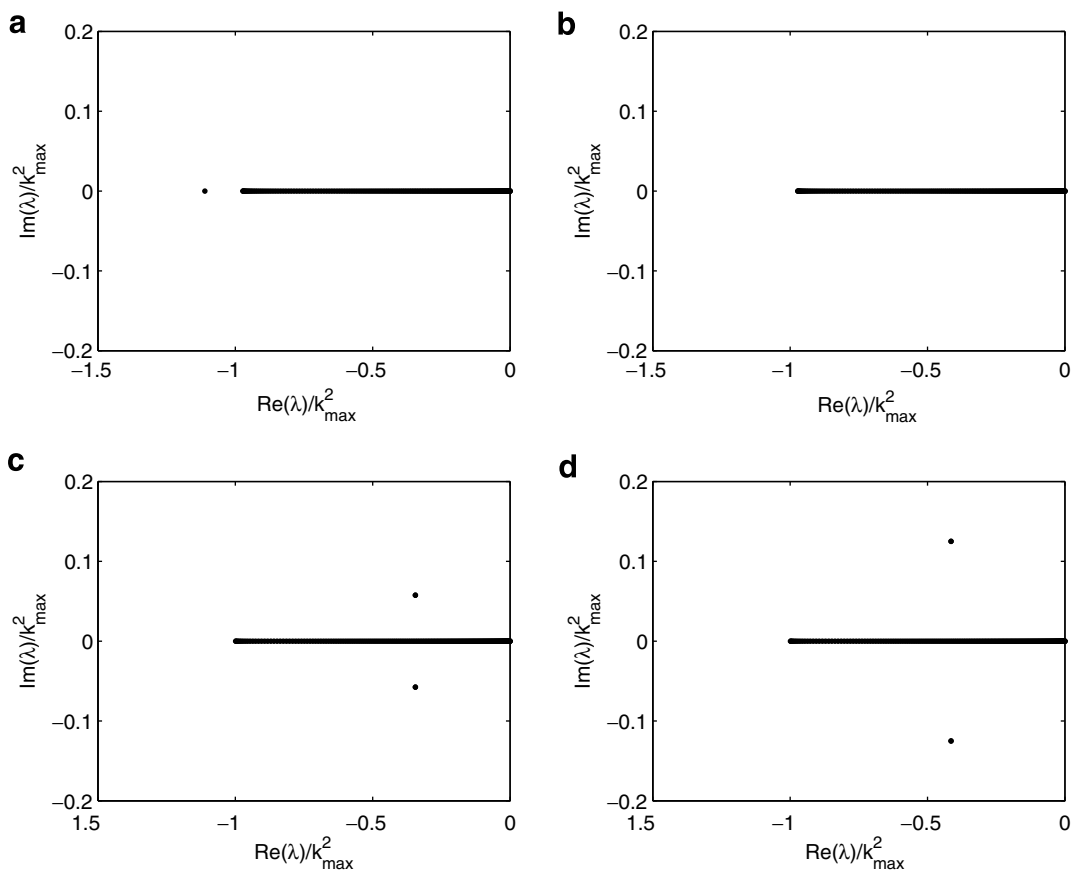


Fig. 10. Distribution of λ/k_{\max}^2 in the complex plane, for: (a) C-D6 + Dirichlet; (b) C-D6 + Neumann; (c) C-D12 + Dirichlet; (d) C-D12 + Neumann.

Distorted, non-orthogonal grids are used for the partition of the square domain. Grids are defined by the following coordinate mapping:

$$\begin{aligned} x &= \frac{1}{2}(\xi_1 + 1) + 0.15\xi_1(1 - \xi_1^2)\xi_2^2 \\ y &= \frac{1}{2}(\xi_2 + 1) - 0.15\xi_1(1 - \xi_2^2)\xi_1^2 \end{aligned} \tag{37}$$

a 20×20 grid generated by the above equations is shown in Fig. 11.

The numerical solution obtained using the proposed high-order method with the face-averaged metric terms computed analytically, is compared against the analytical solution given in Ref. [14]

$$\vartheta(x, y) = \frac{\sinh(\pi y)}{\sinh(\pi)} \sin(\pi x)$$

and a traditional second-order algorithm. The resulting absolute and rms errors attain the expected convergence rate, as shown in Fig. 12.

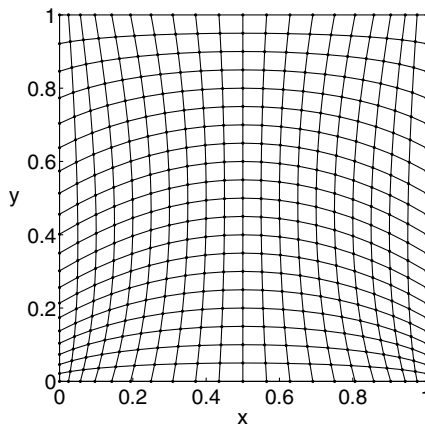


Fig. 11. Distorted grid used for the simulation of the temperature distribution into a flat plate.

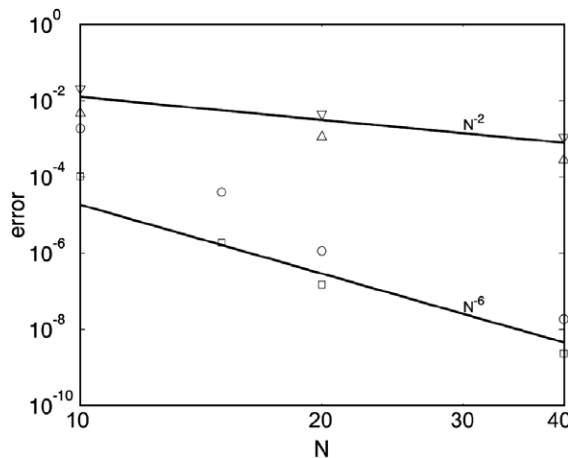


Fig. 12. Absolute and rms errors for problem Section 3.1. \circ : absolute error, C-D6 scheme; \square : rms error, C-D6 scheme; ∇ : absolute error, second-order scheme; \triangle : rms error, second-order scheme.

3.2. Unsteady diffusion

In this section, the simulation of unsteady thermal diffusion is presented in order to provide evidence that the present finite volume formulation can be applied to the solution of time-dependent diffusion phenomena. The physical domain is represented by a plane slab with homogeneous thermal diffusivity. Initially the slab has a uniform temperature distribution T_i . The temperature field evolves in time driven by the heat exchange through the right boundary which is exposed to a fluid of unperturbed temperature T_∞ . The left, upper and lower boundaries are adiabatic. The relevant quantities are scaled by the slab thickness L , the diffusive time-scale L^2/α and the temperature difference $T_i - T_\infty$, yielding to

$$\begin{aligned} \frac{\partial \Theta}{\partial Fo} &= \frac{\partial^2 \Theta}{\partial x^{*2}} + \frac{\partial^2 \Theta}{\partial y^{*2}} \quad (x^*, y^*) \in [0, 1] \\ \Theta(x^*, y^*, Fo = 0) &= 1 \\ \frac{\partial \Theta}{\partial x^*} &= 0 \quad \text{at } x^* = 0, \quad Fo > 0 \\ \frac{\partial \Theta}{\partial x^*} + Bi\Theta &= 0 \quad \text{at } x^* = 1, \quad Fo > 0 \\ \frac{\partial \Theta}{\partial y^*} &= 0 \quad \text{at } y^* = 0, \quad Fo > 0 \\ \frac{\partial \Theta}{\partial y^*} &= 0 \quad \text{at } y^* = 2, \quad Fo > 0 \end{aligned} \tag{38}$$

where $x^* := x/L$, $y^* := y/L$, $\Theta := (T - T_\infty)/(T_i - T_\infty)$, $Fo := \alpha t/L^2$ is the Fourier number, $Bi := hL/k$ is the Biot number. The initial value problem (38) has analytical, one-dimensional solution given in Ref. [14]. Numerical and analytical solutions for a constant Biot number $Bi = 4.0$ are compared over a dimensionless time interval $0 \leq Fo \leq 0.5$.

The rectangular domain is discretized with the distorted grids defined by Eq. (37) and the metrics of the transformation are evaluated analytically. Time integration is performed by an implicit second-order predictor–corrector scheme [1]. During the time integration, the time-step is progressively reduced in order to keep the cell Fourier number $Fo_c := \alpha \Delta t/h^2$ approximately constant.

The relative rms error distributions on a 10×10 and a 20×20 grids are compared in Fig. 13, for the sixth-order C-D and the second-order schemes. After a decrease of the relative error, for $Fo > 0.2$ the error in the solution obtained with the sixth-order method reaches a plateau whereas for the second-order method, due to the damping by numerical diffusion of the initial temperature distribution, the error will grow after $Fo \approx 0.2$.

3.3. Linear free-surface gravity waves

The sloshing of an inviscid liquid under the action of gravity is simulated in a rectangular container and a three-dimensional container with uneven bottom. This is to assess the ability of the algorithm to reproduce an unsteady wave-propagation phenomenon in two and three dimensions. In addition it shows through a relevant physical example that the proposed boundary treatment can handle time-dependent boundary conditions. Under linear approximation, the propagation of surface gravity waves is governed by the following set of equations [5]:

$$\begin{aligned} \mathbf{v} &= \nabla \varphi \\ \nabla^2 \varphi &= 0 \quad \text{in } \overset{\circ}{\Omega} \\ \frac{\partial \varphi}{\partial n} &= 0 \quad \text{on solid surfaces} \\ \frac{\partial \varphi}{\partial t} &= -\eta \quad \text{on free surface } z = 0 \\ \frac{\partial \eta}{\partial t} &= \frac{\partial \varphi}{\partial z} \quad \text{on free surface } z = 0 \end{aligned} \tag{39}$$

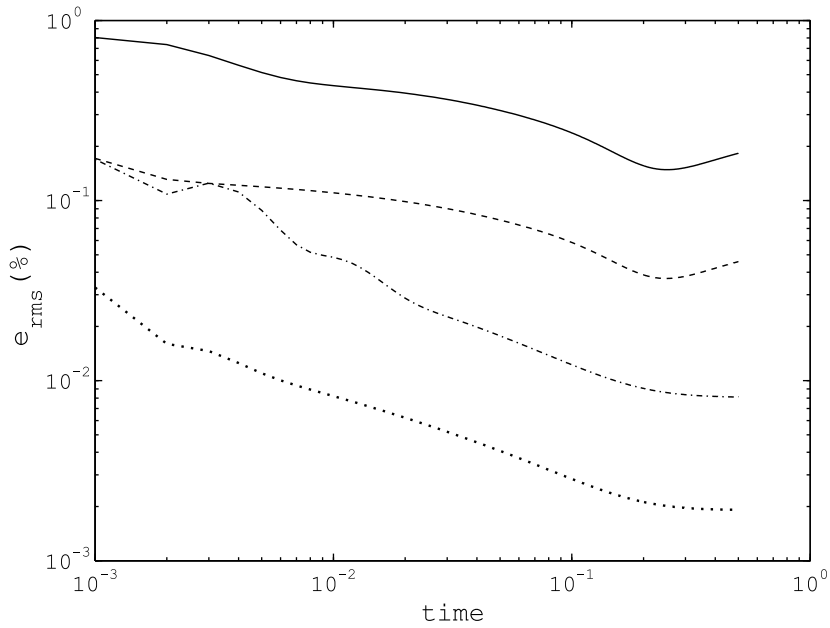


Fig. 13. Relative rms error distribution for the numerical solution of (38). —: second-order scheme on a 10×10 grid; - - -: second-order scheme on a 20×20 grid; - · -: sixth-order scheme on a 10×10 grid; · · ·: sixth-order scheme on a 20×20 grid.

where φ is the velocity potential and η is the elevation of the free surface. Dimensionless quantities are defined by

$$\begin{aligned} x_i^* &:= x_i/H & u_i^* &:= u_i/\sqrt{gH} \\ \varphi^* &:= \varphi/H\sqrt{gH} & t^* &:= t\sqrt{g/H} \end{aligned}$$

in the following, only dimensionless quantities are used, with the asterisk dropped for convenience.

The implicit second-order, three-step predictor–corrector scheme by Akselvoll et al. [1] is used for time-discretization of Eq. (39) yielding, at each substep $k = 0, 1, 2$, the following set of semi-discrete equations:

$$\begin{aligned} \nabla^2 \varphi^{k+1} &= 0 \quad \text{in } \hat{\Omega} \\ \varphi^{k+1} + (\beta^k \Delta t)^2 \frac{\partial \varphi^{k+1}}{\partial n} &= \varphi^k - (\beta^k \Delta t)^2 \frac{\partial \varphi^k}{\partial n} - 2(\beta^k \Delta t) \eta^k \quad \text{on the free surface} \\ \frac{\partial \varphi^{k+1}}{\partial n} &= 0 \quad \text{on solid boundaries} \\ \frac{\partial \varphi^{k+1}}{\partial n} &= 0.01 \cos(2\pi t) \quad \text{on inlet boundary} \\ \eta^{k+1} &= \eta^k + \beta^k \Delta t \left[\frac{\partial \varphi^{k+1}}{\partial z} + \frac{\partial \varphi^k}{\partial z} \right] \quad \text{on the free surface} \end{aligned} \tag{40}$$

where

$$\beta^1 = \frac{4}{15}, \quad \beta^2 = \frac{1}{15}, \quad \beta^3 = \frac{1}{6}$$

The initial surface elevation for both the rectangular and the three-dimensional container is set as

$$\eta(x, t = 0) = \frac{12}{70} \left[1 - \left(\frac{70}{53} x \right)^2 \right] e^{-\left(\frac{70}{76} x\right)^2} \tag{41}$$

3.3.1. Rectangular container

The test is carried out in a two-dimensional rectangular domain of aspect ratio 16/7. Eq. (40) are discretized on a uniform Cartesian mesh and a distorted mesh with 20×15 cells, the latter being represented in Fig. 14.

Fig. 15 shows the surface elevation at different times. On the Cartesian grid, the discrepancy between the surface elevation profiles simulated with the two different algorithms is relatively modest, though increasing

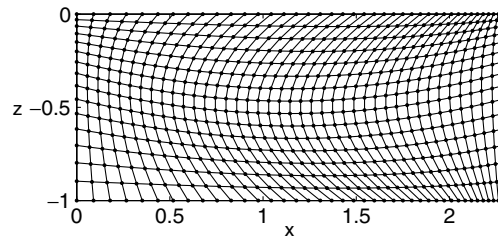


Fig. 14. Distorted grid used for the simulation of sloshing wave propagation through a rectangular container.

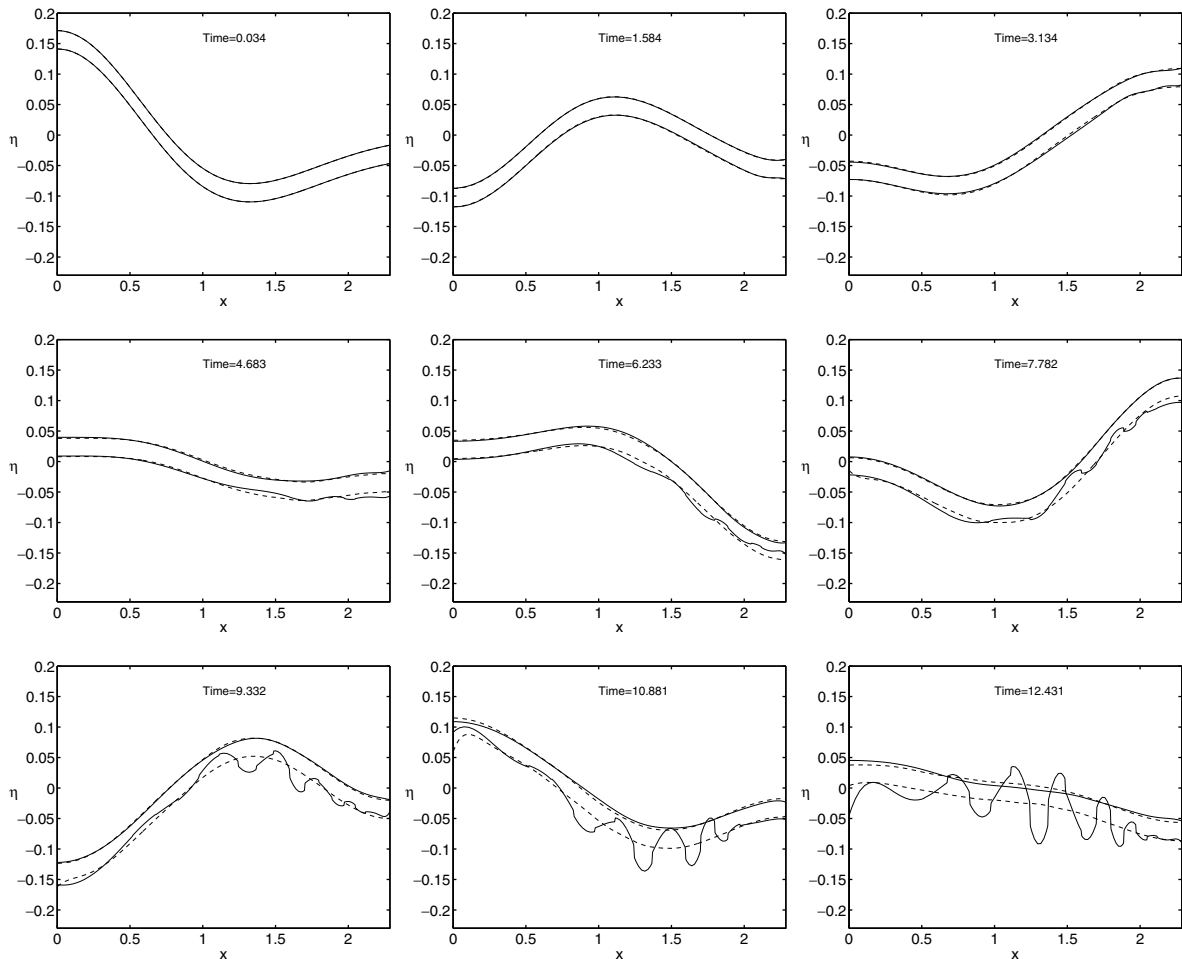


Fig. 15. Propagation of a sloshing wave in a rectangular domain. Surface elevation at different times. Solid lines represent results obtained by the second-order scheme. Dashed lines represent results obtained by the sixth-order C-D scheme. Results obtained on the curvilinear grid are shifted downward by 0.03 units.

with time. While the compact scheme allows to reproduce the correct wave pattern also on the distorted grid, the solution obtained with the second-order scheme develops unphysical ripples for $t \gtrsim 6.0$.

Since mechanical energy is expected to be globally conserved, the imbalance of mechanical energy EI, defined as the relative difference between the time-averaged and the instantaneous mechanical energy may be as well used as an indicator of the quality of the results. Fig. 16 shows the evolution of EI obtained on both the 20×15 Cartesian and distorted meshes with the second-order and the sixth-order C-D schemes. While on the Cartesian grid EI is always bounded, the poor quality of the second-order solution is confirmed on the distorted grid where, unlike the C-D6 results, the imbalance tends to increase monotonically with time.

3.3.2. Three-dimensional container

The uneven bottom of the considered basin is reported in Fig. 17. Tests are carried out on a $30 \times 10 \times 15$ boundary-fitted grid, with the following coordinate mapping:

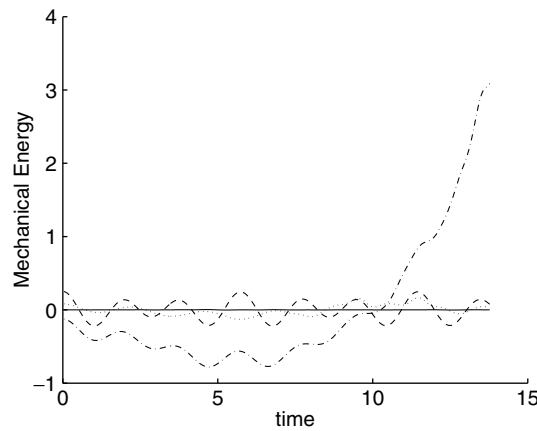


Fig. 16. Imbalance of mechanical energy for the propagation of a sloshing wave through a rectangular container, using a 20×15 mesh. ---: second-order scheme, Cartesian grid; -·-·: second-order scheme, distorted grid (scaled by a factor 0.125); —: sixth-order C-D scheme, Cartesian grid; ···: sixth-order C-D scheme, distorted grid.

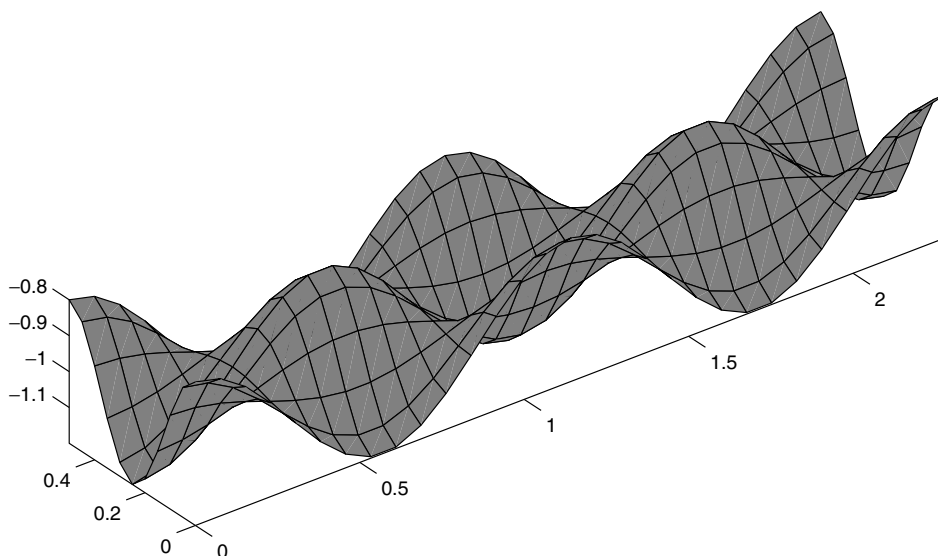


Fig. 17. Bathymetry of the three-dimensional container considered in section 3.3.2.

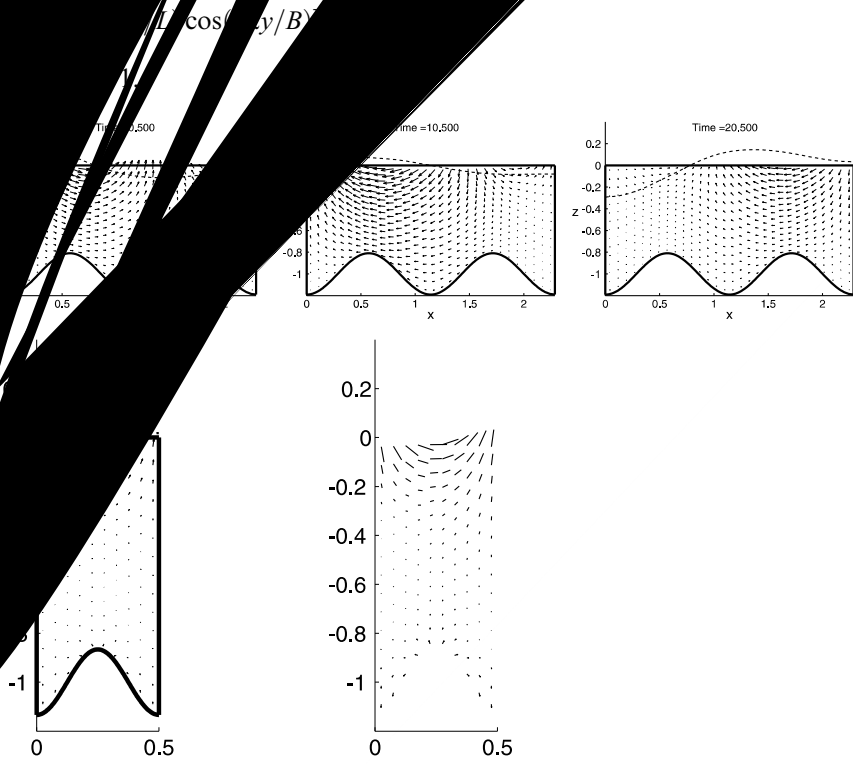


Fig. 18 shows the computed velocity field on selected x - z and y - z planes, at different times. The free-surface elevation is also reported in the figure by a dashed line. Although the flow orientations predicted by the second-order and the sixth-order schemes are very similar, the compact scheme yields higher velocities at all considered sections and times. Differences can also be observed for the computed surface elevation.

In Fig. 19 the EI for the second-order and sixth-order C-D are compared. The root mean square imbalance is 0.6% for the second-order and 0.01% for the sixth-order schemes, on such a very coarse grid.

The distribution of φ and the surface elevation on the x - z mid-plane, at time $t = 6.65$, are compared for two different grid resolutions in Fig. 20. The considered grids have $30 \times 10 \times 15$ and $60 \times 20 \times 30$ control volumes, respectively. Only small differences can be detected between the two scalar fields, while the elevations match almost perfectly.

3.4. Rotation of a sharp scalar cone

A common test for numerical solvers of hyperbolic equations is the advection of a sharp scalar cone around a circular path. The initial distribution of the scalar in a $[-2, 2] \times [-2, 2]$ square domain is given as

$$\varphi(x, y) = e^{-(r/r_0)^2}$$

where $r = \sqrt{(x - 1)^2 + y^2}$ and $r_0 = 0.2$. The scalar field is advected by a imposed steady velocity field

$$\mathbf{u} = (-y, x)2\pi/T$$

where $T = 10$ is the revolution time period.

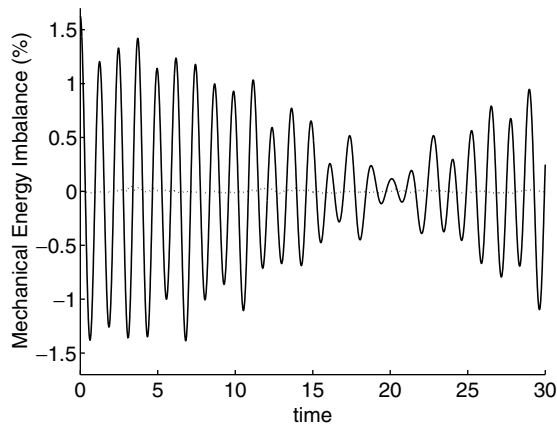


Fig. 19. Trace of mechanical energy imbalance. \cdots : Sixth-order C-D scheme and $—$: second-order scheme.

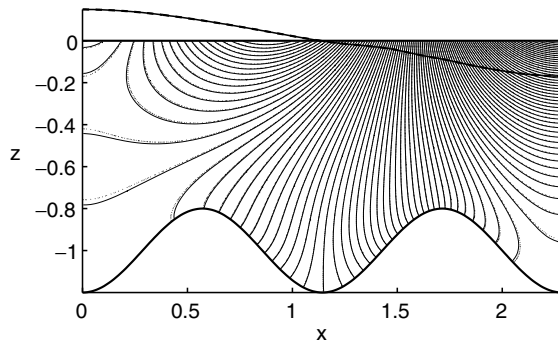


Fig. 20. Comparison of φ and surface elevation for the three-dimensional sloshing-wave problem. Solid lines: grid $30 \times 10 \times 15$; dashed lines: grid $60 \times 20 \times 30$.

The coordinate mapping is defined as

$$\begin{aligned} x &= 2, (\xi_1 + 1) + 0.65\xi_1(1 - \xi_1^2)\xi_2^2 - 2 \\ y &= 2(\xi_2 + 1) - 0.65(1 - \xi_2^2)\xi_1^2 - 2 \end{aligned} \quad (43)$$

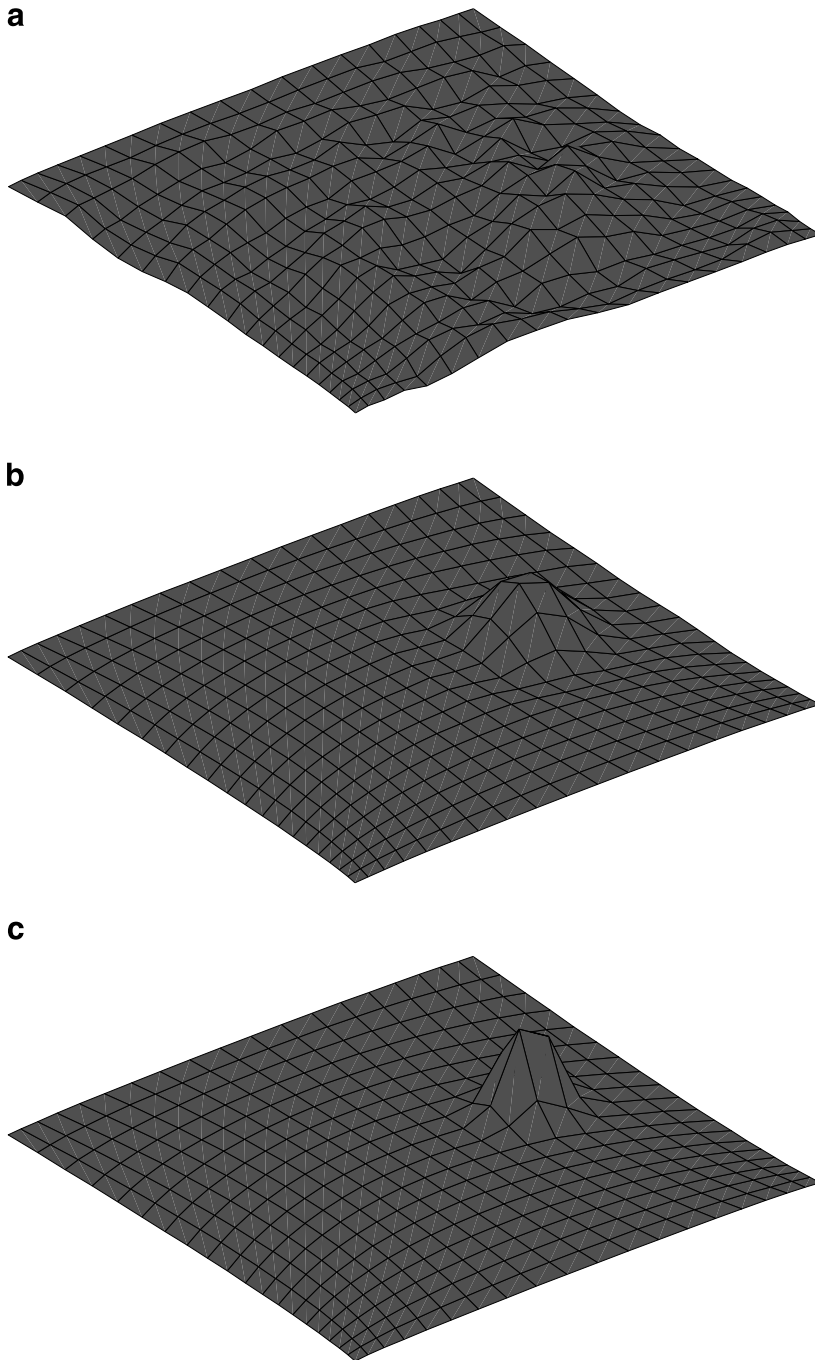


Fig. 21. Distribution of a $\bar{\varphi}$ (averaged on control volumes in computational space) after a complete revolution on a 20×20 grid. (a) Second-order finite volume method at $t = T$; (b) fifth-order compact finite volume method at $t = T$; and (c) initial distribution.

Homogeneous Dirichlet boundary conditions are enforced at the cell faces located on inflow portions of the boundary, while there is no need to enforce outflow boundary conditions.

The scalar distribution at $t = T/10$ and $t = T$ is shown in Figs. 21 and 22 for a 20×20 and a 40×40 distorted grid, respectively. After one complete revolution the solution computed on the 20×20 grid by the proposed high-order method, including the spatial discretization scheme proposed by Pirozzoli [26], is only slightly diffused and almost oscillation-free. On the other hand, the second-order method is seriously affected

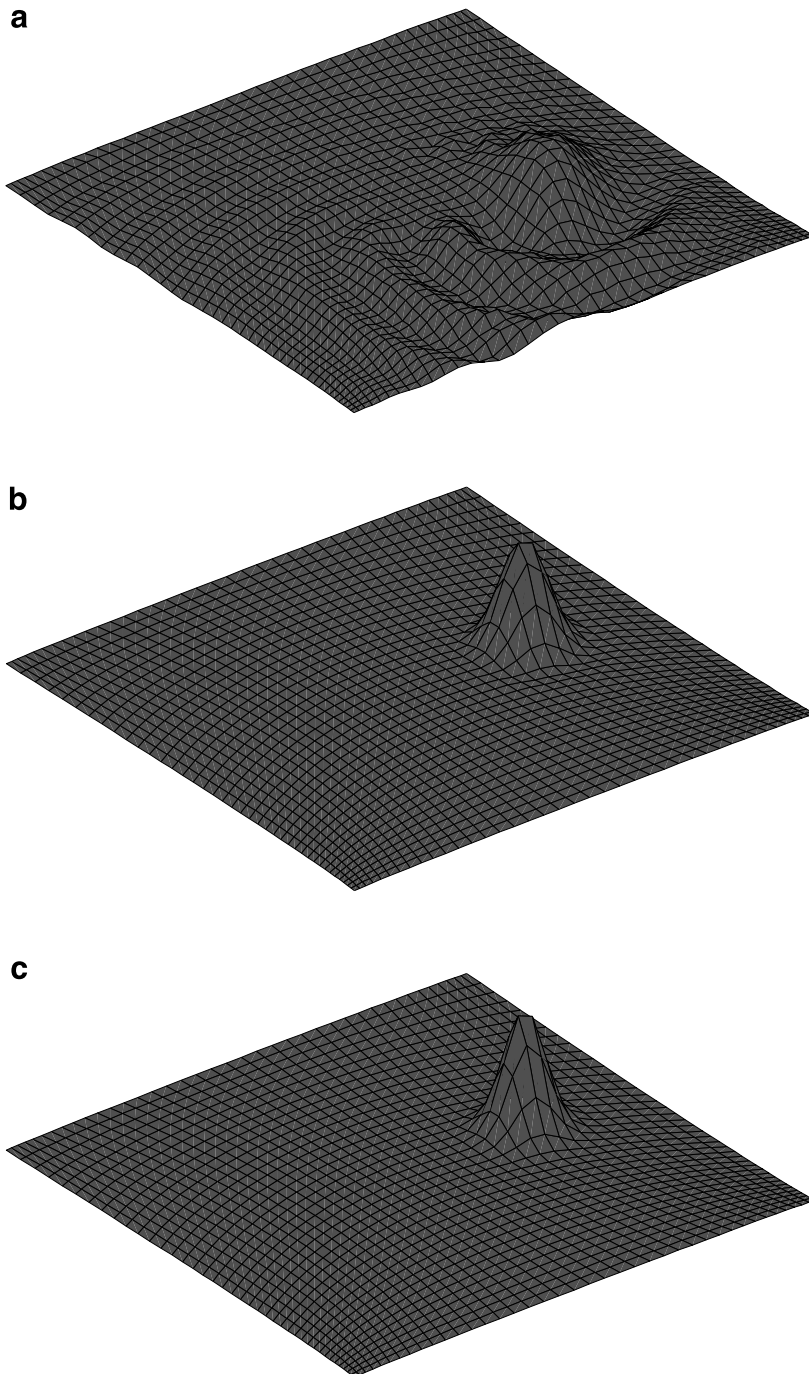


Fig. 22. Distribution of a $\bar{\varphi}$ (averaged on control volumes in computational space) after a complete revolution on a 40×40 grid. (a) Second-order finite volume method at $t = T$; (b) fifth-order compact finite volume method at $t = T$; and (c) initial distribution.

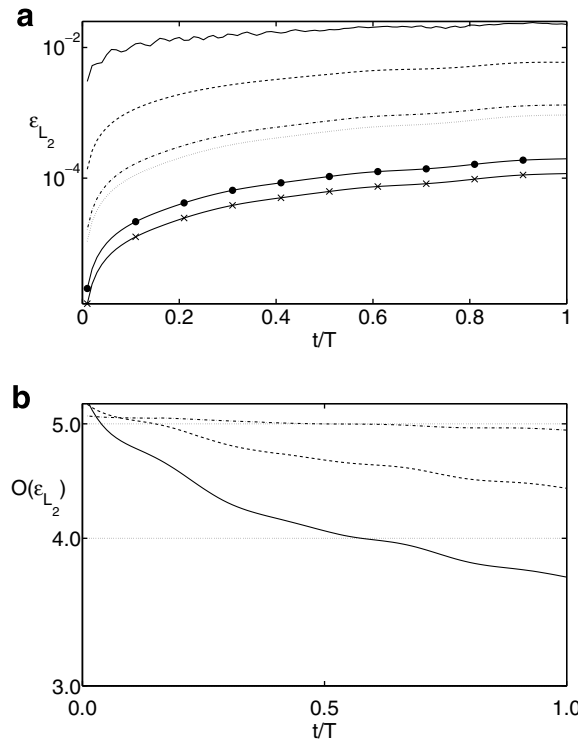


Fig. 23. (a) L_2 error and (b) convergence rate for the rotation of a sharp scalar cone, the latter computed by comparing errors on couples of different grids. Symbols in (a): — for the 20×20 grid; --- for the 40×40 grid; -·- for the 60×60 grid; ···· for the 65×65 grid; —●— for the 90×90 grid; —×— for the 100×100 grid. Symbols in (b): — for the couple $(40 \times 40, 60 \times 60)$; --- for the couple $(60 \times 60, 65 \times 65)$; -·- for the couple $(90 \times 90, 100 \times 100)$.

by dispersion errors and the initial scalar distribution is soon converted into broad spectrum noise also on the 40×40 grid.

A systematic study of convergence is carried out on a hierarchy of refined meshes. The L_2 error on $\overline{\varphi}^{\varepsilon_1 \varepsilon_2}$ and the associated convergence rate are shown in Fig. 23, showing that the present method yields fifth-order asymptotic convergence. The considered meshes use 20×20 , 40×40 , 60×60 , 65×65 , 90×90 and 100×100 cells. The convergence rates are computed by comparing the error on couples of near meshes.

4. Concluding remarks

A compact finite volume method for the scalar advection–diffusion equation on three-dimensional curvilinear grids is developed. In the present work a sixth-order composite template, based on a symmetric C-D interior scheme and explicit boundary schemes, is used for the discretization of the diffusive fluxes, while the fifth-order upwind compact template proposed by Pirozzoli [26] is selected to approximate the advective fluxes.

The sixth-order template is investigated using the technique proposed by Jordan [16], showing very high resolution except for the first one or two control volumes near the boundary. In spite of this favorable characteristic, it is found that C-D schemes become progressively more ill conditioned as the computational grid is refined.

The proposed methodology is aimed to form a basis for further application to the Navier–Stokes equations, with the possibility of accommodating either explicit or compact schemes of arbitrary accuracy, different high-order deconvolution and flux-reconstruction schemes and general boundary conditions.

Acknowledgment

The authors are grateful to Professor Pierpaolo Omari for remarks on a draft of this paper.

Appendix A. Mathematical details of the Fourier analysis

The finite volume representation of Eq. (29) reads

$$\frac{\partial \bar{\varphi}_j}{\partial t} h = \alpha \left[\frac{\delta \varphi}{\delta x} \Big|_{j+1/2} - \frac{\delta \varphi}{\delta x} \Big|_{j-1/2} \right] \quad j = 0, \dots, N - 1 \tag{A.1}$$

where $\delta/\delta x$ denotes numerical differentiation and N is the number of cells used to discretize the domain. The system of Eq. (A.1) can be represented in matrix form as

$$h \frac{\partial \{\bar{\varphi}\}}{\partial t} = \alpha [A] \left\{ \frac{\delta \varphi}{\delta x} \right\} \tag{A.2}$$

where

$$\{\bar{\varphi}\} \equiv \{\bar{\varphi}_1, \dots, \bar{\varphi}_N\}^t \quad \left\{ \frac{\delta \varphi}{\delta x} \right\} \equiv \left\{ \frac{\delta \varphi}{\delta x} \Big|_{3/2}, \dots, \frac{\delta \varphi}{\delta x} \Big|_{N+1/2} \right\}^t$$

$$[A] \equiv \begin{bmatrix} 1 & 0 & \dots & 0 & -1 \\ -1 & 1 & 0 & & 0 \\ \dots & \dots & \dots & \dots & \dots \\ \dots & \dots & \dots & \dots & \dots \\ \dots & \dots & \dots & \dots & \dots \\ \dots & \dots & \dots & \dots & \dots \\ 0 & \dots & \dots & 0 & -1 & 1 \end{bmatrix}$$

Due to the periodic nature of the problem, the matrix $[A]$ is circulant [7]. The discrete difference operator may be represented in matrix form as

$$[N]\{\varphi\} + h[M]\left\{ \frac{\delta \varphi}{\delta x} \right\} = [D]\{\bar{\varphi}\} \tag{A.3}$$

where $[N]$, $[M]$, $[D]$ are $2N \times N$ block-circulant matrices. $\{\delta \varphi/\delta x\}$ can be obtained from (A.3) as a function of $\{\bar{\varphi}\}$.

$$\begin{aligned} [N] &= \begin{bmatrix} [N_1] \\ [N_2] \end{bmatrix} & [M] &= \begin{bmatrix} [M_1] \\ [M_2] \end{bmatrix} & [D] &= \begin{bmatrix} [D_1] \\ [D_2] \end{bmatrix} \\ h[\tilde{M}]\left\{ \frac{\delta \varphi}{\delta x} \right\} &= [\tilde{D}]\{\bar{\varphi}\} & \left\{ \frac{\delta \varphi}{\delta x} \right\} &= \frac{1}{h} [\tilde{M}]^{-1} [\tilde{D}]\{\bar{\varphi}\} \\ [\tilde{M}]^{-1} [\tilde{D}] &= ([M_1] - [N_1][M_2][N_2]^{-1})^{-1} ([D_1] - [N_1][D_2][N_2]^{-1}) \end{aligned}$$

Since the matrix inverse, the matrix product and the matrix summation of circulant matrices yield circulant matrices [7], it turns out that $[\tilde{M}]^{-1}[\tilde{D}]$ is circulant.

With the above definitions, Eq. (A.2) can be recast as

$$\frac{\partial\{\bar{\varphi}\}}{\partial Fo} = [A][\tilde{M}]^{-1}[\tilde{D}]\{\bar{\varphi}\} \tag{A.4}$$

Recalling that the eigenvectors of any circulant matrix of order N are [7]

$$\{e^{-i2\pi kj/N}\}_{j=0}^{N-1} \quad k = 0, \dots, N - 1$$

the solution at *time* Fo can be expanded with respect to the basis of eigenvectors, plugged into Eq. (A.4) and solved for, yielding

$$\bar{\varphi}_j(Fo) = \sum_{k=0}^{N-1} \sigma_k(Fo) F(K) e^{-i2\pi kj/N} \quad \sigma_k(Fo) = \sigma_k(0) e^{\lambda_k Fo} \tag{A.5}$$

where λ_k denotes the k th eigenvalue of $[A][\tilde{M}]^{-1}[\tilde{D}]$. Comparing Eqs. (A.5) and (30) it is evident that the error between the numerical and analytical solutions can be characterized by the error function, defined as

$$E(K) \equiv -\frac{\lambda_k}{K^2} \tag{A.6}$$

The eigenvalues λ_k can be obtained as follows:

$$\lambda_k = \lambda_k([A]) \frac{\lambda_k([\tilde{D}])}{\lambda_k([\tilde{M}])} = \lambda_k([A]) \frac{\lambda_k([N_2])\lambda_k([D_1]) - \lambda_k([N_1])\lambda_k([D_2])}{\lambda_k([M_1])\lambda_k([N_2]) - \lambda_k([N_1])\lambda_k([M_2])} \tag{A.7}$$

The eigenvalues of a circulant matrix are the Discrete Fourier Transforms of the first row (or column) of the matrix [7]. For tri-diagonal matrices, as those in Eq. (A.7), a simpler identity holds [20]

$$\lambda_k = \beta + (\alpha + \gamma) \cos(K) - i(\alpha - \gamma) \sin(K) \tag{A.8}$$

where α , β , γ are the subdiagonal, diagonal and superdiagonal matrix entries, respectively.

Using the above results, the error function has been computed for several finite volume schemes:

- Second-order finite volume scheme (FV2 hereafter)

$$\left. \frac{\delta\varphi}{\delta x} \right|_{j+1/2} \equiv \frac{\bar{\varphi}_{j+1} - \bar{\varphi}_j}{h} \tag{A.9}$$

$$E(K) = 2 \frac{1 - \cos(K)}{K^2} \tag{A.10}$$

- Fourth-order Padé finite volume scheme (CFV4 hereafter) [24]

$$\frac{1}{10} \left. \frac{\delta\varphi}{\delta x} \right|_{j-1/2} + \left. \frac{\delta\varphi}{\delta x} \right|_{j+1/2} + \frac{1}{10} \left. \frac{\delta\varphi}{\delta x} \right|_{j+3/2} = \frac{6}{5} \frac{\bar{\varphi}_{j+1} - \bar{\varphi}_j}{h} \tag{A.11}$$

$$E(K) = 24 \frac{[\sin(K/2)]^2}{K^2(5 + \cos(K))} \tag{A.12}$$

- Fourth-order *spectral-like* finite volume scheme (SCFV4 hereafter) [25]

$$0.226 \left. \frac{\delta\varphi}{\delta x} \right|_{j-1/2} + \left. \frac{\delta\varphi}{\delta x} \right|_{j+1/2} + 0.226 \left. \frac{\delta\varphi}{\delta x} \right|_{j+3/2} = 1.137 \frac{\bar{\varphi}_{j+1} - \bar{\varphi}_j}{h} + 0.105 \frac{\bar{\varphi}_{j+2} - \bar{\varphi}_{j-1}}{h} \tag{A.13}$$

$$E(K) = -\frac{3}{2} \frac{35 \cos(2K) + 344 \cos(K) - 379}{[250 + 113 \cos(K)]K^2} \tag{A.14}$$

- Present sixth-order C-D scheme.

$$0.4375\varphi_{j-1/2} + \varphi_{j+1/2} + 0.4375\varphi_{j+3/2} + 0.0625h \left[\frac{\delta\varphi}{\delta x} \Big|_{j-1/2} - \frac{\delta\varphi}{\delta x} \Big|_{j+3/2} \right] = 0.9375[\bar{\varphi}_{j+1} + \bar{\varphi}_j] \quad (\text{A.15})$$

$$- 1.125\varphi_{j-1/2} + 1.125\varphi_{j+3/2} + h \left[-0.125 \frac{\delta\varphi}{\delta x} \Big|_{j-1/2} + \frac{\delta\varphi}{\delta x} \Big|_{j+1/2} - 0.125 \frac{\delta\varphi}{\delta x} \Big|_{j+3/2} \right] = 3[\bar{\varphi}_{j+1} - \bar{\varphi}_j] \quad (\text{A.16})$$

$$E(K) = 3 \frac{\sin(K/2)}{K^2} \frac{11 \sin(3K/2) + 27 \sin(K/2)}{2[\cos(K)]^2 + 23 + 20 \cos(K)} \quad (\text{A.17})$$

References

- [1] K. Akselvoll, P. Moin, An efficient method for temporal integration of the Navier–Stokes equations in confined axisymmetric geometries, *J. Comp. Phys.* 125 (1996) 454.
- [2] B.J. Boersma, A staggered compact finite difference formulation for the compressible NavierStokes equations, *J. Comp. Phys.* 208 (2005) 675.
- [3] C. Canuto, M.Y. Hussaini, A. Quarteroni, T.A. Zang, *Spectral Methods in Fluid Dynamics*, Springer-Verlag, New York, USA, 1988.
- [4] A.K. De, V. Eswaran, Analysis of a new high resolution upwind compact scheme, *J. Comp. Phys.* 218 (2006) 398.
- [5] R.G. Dean, R.A. Dalrymple, *Water Wave Mechanics for Engineers and Scientists*, World Scientific, London, UK, 2000.
- [6] L. Gamet, F. Ducros, F. Nicoud, T. Poinso, Compact finite difference schemes on non-uniform meshes. Application to direct numerical simulation of compressible flows, *Int. J. Numer. Meth. Fluids* 29 (1999) 159.
- [7] R.M. Gray, *Toeplitz and Circulant Matrices: A Review*, Now Publishers, Hanover, MA, USA, 2006.
- [8] B. Gustafsson, The convergence rate for difference approximations to mixed initial boundary value problems, *Math. Comput.* 29 (130) (1975) 396.
- [9] R. Hixon, Prefactored small-stencil compact schemes, *J. Comp. Phys.* 165 (2000) 522.
- [10] G.E. Karniadakis, S.I. Sherwin, *Spectral/hp Element Methods for CFD*, Oxford University Press, Oxford, UK, 1998.
- [11] F. Keiderling, S.B. Müller, L. Kleiser, A high-fidelity numerical method for the simulation of compressible flows in cylindrical geometries, *Proc. Appl. Math. Mech.* 4 (2004) 572–573.
- [12] M.H. Kobayashi, On a class of Padé finite volume methods, *J. Comp. Phys.* 156 (1999) 137.
- [13] W.Y. Kwok, R.D. Moser, J. Jiménez, A critical evaluation of the resolution properties of B-spline and compact finite difference methods, *J. Comp. Phys.* 174 (2001) 510.
- [14] F.P. Incropera, D.P. DeWitt, *Fundamentals of Heat and Mass Transfer*, Wiley & Sons, New York, 1996.
- [15] L. Jiang, C. Liu, Applications of weighted compact scheme to curvilinear coordinate system, in: *Proceedings of the Fifth International Conference on Numerical Methods Applications*, Borovets, Bulgaria, 2002.
- [16] S.A. Jordan, The spatial resolution properties of composite compact finite differencing, *J. Comp. Phys.* 221 (2007) 558.
- [17] C. Lacor, S. Smirnov, M. Baelmans, A finite volume formulation of compact central schemes on arbitrary structured grids, *J. Comp. Phys.* 198 (2004) 535.
- [18] S.K. Lele, Compact finite difference schemes with spectral-like resolution, *J. Comp. Phys.* 103 (1992) 16.
- [19] C. Liu, High performance computation for DNS/LES, *Appl Math. Model.* 30 (10) (2006) 1143.
- [20] H. Lomax, T.H. Pulliam, D.W. Zingg, *Fundamentals of Computational Fluid Dynamics*, Springer, Berlin, 2001.
- [21] K. Mahesh, A family of high-order finite difference schemes with good spectral resolution, *J. Comp. Phys.* 145 (1998) 332.
- [22] S. Mallat, *A Wavelet Tour of Signal Processing*, Academic Press, San Diego, CA, USA, 1999.
- [23] B. Mattiussi, An analysis of finite-volume, finite-element, and finite-difference methods using some concepts from algebraic topology, *J. Comp. Phys.* 133 (2) (1997) 289.
- [24] J.M.C. Pereira, M.H. Kobayashi, J.C.F. Pereira, A fourth-order-accurate finite volume compact method for the incompressible Navier–Stokes solutions, *J. Comp. Phys.* 167 (2001) 217.
- [25] M. Piller, E. Stalio, Finite volume schemes on staggered grids, *J. Comp. Phys.* 197 (2004) 299.
- [26] S. Pirozzoli, Conservative hybrid compact-WENO schemes for shock–turbulence interaction, *J. Comp. Phys.* 178 (2002) 81.
- [27] M. Popescu, W. Shyy, M. Garbey, Finite volume treatment of dispersion-relation-preserving and optimized prefactored compact schemes for wave propagation, *J. Comp. Phys.* 210 (2005) 705.
- [28] T.K. Sengupta, R. Jain, A. Dipankar, A new flux-vector splitting compact finite volume scheme, *J. Comp. Phys.* 207 (2005) 261.
- [29] C. Sung, L. Jiang, C. Liu, Application of high-order compact scheme in a computer flow solver for incompressible Reynolds-averaged Navier–Stokes equations, in: *Proceedings of the Third AFOSR International Conference on DNS/LES*, UTA, 2001.
- [30] R. Vichnevetsky, J.B. Bowles, *Fourier Analysis of Numerical Approximations of Hyperbolic Equations*, Studies in Applied Mathematics, SIAM, Philadelphia, 1982.
- [31] B. Wright, Scattered node compact finite difference-type formulas generated from radial basis functions, *J. Comp. Phys.* 212 (2006) 99.
- [32] K.K.Q. Zhang, B. Shotorban, W.J. Minkowycz, F. Mashayek, A compact finite difference method on staggered grid for Navier–Stokes flows, *Int. J. Numer. Meth. Fluids* 52 (2006) 867.